BRNO UNIVERSITY OF TECHNOLOGY

VYSOKÉ UČENÍ TECHNICKÉ V BRNĚ

FACULTY OF MECHANICAL ENGINEERING

FAKULTA STROJNÍHO INŽENÝRSTVÍ

INSTITUTE OF PHYSICAL ENGINEERING

ÚSTAV FYZIKÁLNÍHO INŽENÝRSTVÍ

QUANTUM INFORMATION AND SUPERCONDUCTING CIRCUITS

KVANTOVÁ INFORMACE A SUPRAVODIVÉ OBVODY

MASTER'S THESIS

DIPLOMOVÁ PRÁCE

AUTHOR — BA Katerina Stloukalova

AUTOR PRÁCE

SUPERVISOR — Mgr. Jakub Bělín, Ph.D.

VEDOUCÍ PRÁCE

BRNO 2024

BRNO UNIVERSITY OF TECHNOLOGY
FACULTY OF MECHANICAL ENGINEERING

Assignment Master's Thesis

Institut:	Institute of Physical Engineering
Student:	**BA Katerina Stloukalova**
Degree programm:	Precise Mechanics and Optics
Branch:	no specialisation
Supervisor:	**Mgr. Jakub Bělín, Ph.D.**
Academic year:	2023/24

As provided for by the Act No. 111/98 Coll. on higher education institutions and the BUT Study and Examination Regulations, the director of the Institute hereby assigns the following topic of Master's Thesis:

Quantum Information and Superconducting Circuits

Brief Description:

Quantum computers are novel devices whose fundamental working principle is based on the laws of quantum physics. The main idea is to exploit special quantum effects for a unique computing paradigm. There exist several hardware platforms for the experimental realization of a quantum computer. Superconducting circuits are among the most popular hardware realization. Here, electric chips are fabricated based on superconducting material and cooled down for the operation in the quantum regime. The properties of those chips depend on the exact configuration and specification of the electric elements which are deposed on the chip.

Master's Thesis goals:

Study of the fundamental physical principles concerning superconducting qubits, as well as developing numerical optimization tools.
Automated optimization of superconducting circuits.

Recommended bibliography:

NIELSEN, Michael A. a Isaac L. CHUANG. Quantum Computation and Quantum Information. Cambridge: Cambridge University Press, 2012. ISBN 9781107002173. Dostupné z: doi:10.1017/CBO9780511976667

LANGFORD, Nathan K. Circuit qed-lecture notes. 2013. arXiv preprint arXiv:1310.1897.

KRANTZ, Philip, Morten KJAERGAARD, Fei YAN, Terry P. ORLANDO, Simon GUSTAVSSON a William D. OLIVER. A quantum engineer's guide to superconducting qubits. Applied Physics Reviews. 2019, 2019-06-01, 6(2). ISSN 1931-9401. Dostupné z: doi:10.1063/1.5089550

VOOL, Uri a DEVORET, Michel. Introduction to quantum electromagnetic circuits. Online. International Journal of Circuit Theory and Applications. 2017, roč. 45, č. 7, s. 897-934. ISSN 0098-9886. Dostupné z: https://doi.org/10.1002/cta.2359.

RASMUSSEN, S.E.; CHRISTENSEN, K.S.; PEDERSEN, S.P.; KRISTENSEN, L.B.; BÆKKEGAARD, T. et al. Superconducting Circuit Companion—an Introduction with Worked Examples. Online. PRX Quantum. 2021, roč. 2, č. 4. ISSN 2691-3399. Dostupné z: https://doi.org/10.1103/PRXQuantum.2.040204.

Deadline for submission Master's Thesis is given by the Schedule of the Academic year 2023/24

In Brno,

L. S.

prof. RNDr. Tomáš Šikola, CSc. Director of the Institute	doc. Ing. Jiří Hlinka, Ph.D. FME dean

Abstrakt
Snaha o stabilní qubity v kvantovém zpracování informací přitahuje značnou pozornost, zejména v supravodivých obvodech známých svým potenciálem zvýšit koherenční čas. Projekt "Numerická optimalizace supravodivých obvodů" řeší problémy nákladného experimentování a využívá software Scoptimization. Testování na známých qubitech jako Transmon a Fluxonium byly identifikovány optimální hodnoty s vylepšeným časem. Obecné testování obvodů navíc odhalilo, že Fluxonium (T4) se ukázalo jako vítěz s nejdelším časem, což dále zdůraznilo jeho potenciál pro pokrok ve výzkumu qubitů. Fluxonium zejména dosáhlo koherenční doby 2,7 milisekundy, čímž překonalo dříve pozorovanou experimentální hodnotu 1,48 milisekundy.

Abstract
The pursuit of stable qubits in quantum information processing garners significant attention, particularly in superconducting circuits known for their potential to enhance coherence time. Addressing the challenges of costly experimentation, the "Numerical optimization of superconducting circuits" project utilizes Scoptimization software. The Python package identifies optimal circuit values when testing established qubits like Transmon and Fluxonium. General circuit testing revealed that Fluxonium (T4) emerged as the winner, further highlighting its potential for advancing qubit research. Additionally, Fluxonium notably achieved a coherence time of 2.7 milliseconds, surpassing the previously observed experimental value of 1.48 milliseconds.

Klíčová slova
Supravodivé obvody, Transmon, Fluxonium, SQUID, Flux Qubit, Scoptimization, Numerická optimalizace qubitů, optimalizace různých variací supravodivých obvodů, qubitově optimalizované Hamiltonovské parametry, qubity definovaná anharmonicita, porovnání koherenční doby pro různé supravodivé obvody.

Keywords
Superconducting circuits, Transmon, Fluxonium, SQUID, Flux Qubit, Scoptimization, Numerical optimization of qubits, general superconducting circuit optimization, qubit's optimized Hamiltonian energy parameters, qubits defined anharmonicity, comparison of coherence time for different superconducting circuit parameters.

STLOUKALOVA, K. *Quantum Information and Superconducting Circuits.*. Brno: Brno University of Technology, Faculty of Mechanical Engineering, 2024. 12 s. Supervised by Mgr. Jakub Bělín, Phd.

I hereby affirm that this master's thesis is the result of my independent effort, with guidance from my supervisor. All references and sources utilized in this work have been duly acknowledged and cited.

BA. Katerina Stloukalova

I would like to express my deepest gratitude to my supervisor, **Jakub Bělín**, for his invaluable support and encouragement in pursuing the topic of my master's thesis. His guidance, patience, and insightful communication have been instrumental not only for this thesis but also as lessons I will carry forward into the next chapter of my life. I am also immensely grateful to **Philipp Aumann** and **Berend Klaver** from the University of Innsbruck for their collaboration and assistance. Their inclusion of me in their project, which became the basis of my master's thesis, significantly expanded my knowledge of quantum computing and opened new doors for my future career.

I extend my appreciation to all those who took the time to advise and support me on various topics, contributing to the successful completion of this thesis, especially my classmate **Klára Stříbrná**.

A special thank you goes to my mother, **Hana Stloukalová**, whose unwavering support and understanding have been invaluable. Her incredible patience and the immense amount of energy she invested in supporting me cannot be adequately described. Lastly, I wish to thank my grandparents, **Zita** and **Ivo Winklerovi**, and friends for their advice and patience throughout this journey. Your support has been crucial in helping me reach this point.

This work was performed with the support of ParityQC and the University of Innsbruck.

BA. Katerina Stloukalova

Contents

Introduction

Quantum computing and information are at the forefront of investment interests, with businesses increasingly influenced by remarkable advancements that bridge quantum phenomena with classical technology [1]. This surge in interest has led to significant financial contributions to the field. The pursuit of national security has intensified, driven by the potential of quantum computers to solve unsolvable problems [2]. However, cybersecurity concerns persist. Despite the challenges, constructing quantum computers is now within reach, albeit demanding precise assembly of delicate components. Superconducting circuits and trapped ions are favored for their longer coherence times [3], playing pivotal roles in qubit construction, as depicted in Figure 1.

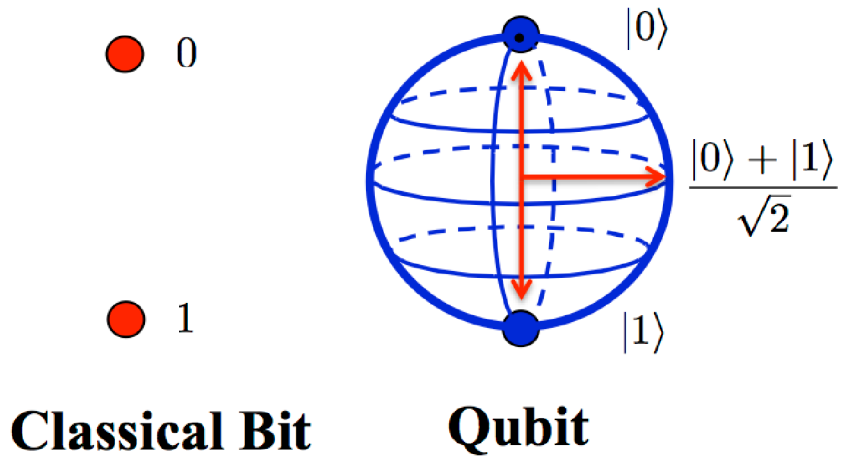

Figure 1: The image represents classical bits on the left side, symbolized as 0 or 1, while the right side illustrates a qubit's representation on the Bloch sphere, which can exist simultaneously as 0 and 1. Utilizing the sphere aids in visualizing the spatial superposition of the qubit. Image taken from [4].

Classical computers utilize bits, representing 0 or 1, as the basic unit of information. Quantum computers employ qubits with similar roles but distinct properties arising from quantum phenomena like superposition, enabling them to exist in multiple states simultaneously until measured [5]. A multi-qubit system is essential to enhance quantum computing capabilities for more extensive and complex operations. Such a system must manage superposition and harness entanglement among qubits, a crucial aspect [5]. This behavior enables parallel computation, speeding up unsolved math problems or cryptographic algorithms like Shor's or Grover's [6]. If a hostile nation gets a quantum computer, it could pose a significant national threat, contingent on qubit stability and cooperation.

The best method for designing qubits is using circuit QED devices, which exploit quantum dynamics in superconducting circuits. These circuits benefit mainly from a significant component called the Josephson junction (more details in Section 1.2), which introduces a non-linear aspect to the entire system [7]. Thus, it is possible to realize the concept of an artificial atom. As a result, it enables quantum properties such as superposition and, in multi-qubit systems, entanglement.

Understanding the transfer of quantum properties to the macroscopic realm involves mathematical analogies between qubit circuit design, quantum harmonic oscillators, and LC circuits, aiding in deriving a Hamiltonian [7]. This framework effectively describes qubit circuit dynamics and their interaction with the environment, which is essential for analyzing and optimizing superconducting circuits. Improved qubits are achieved by altering physical properties, remarkably to reduce system noise, a key challenge in maintaining qubit coherence [8]. Strategies to mitigate various types of noise have been developed, including modifying circuit elements to extend qubit lifetime, a focal point of this project.

Figure 2 illustrates the progress of different qubits in terms of their lifetime and the year of their discovery or development. Each qubit features a particular Hamiltonian tailored to its specific circuit configuration and characteristics. A crucial characteristic is the coherence time (T_2 and T_1), which needs to be as long as possible to ensure. Figure 2 demonstrates that while there has been advancement in the lifetime of qubits, it is still insufficient to realize the full potential of quantum computing.

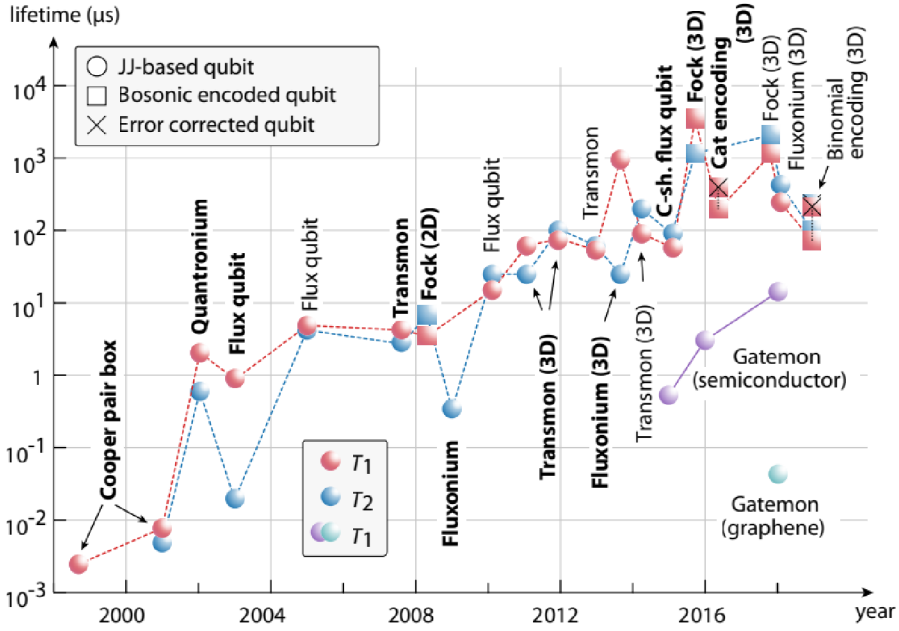

Figure 2: The graph illustrates the evolution of lifetime and coherence times in various superconducting circuits. It displays a timeline depicting the progression of coherence times corresponding to the development and adjustments of qubits. The Figure displays three distinct qubit types: Josephson junction (JJ) based, bosonic encoded qubit, and error-corrected qubit. While the Transmon qubit exhibits the longest longitudinal relaxation time T_1, the Fluxonium qubit has the longest coherence time T_2, which is particularly important for the project focusing on JJ-type qubits. Image taken from [9].

The discovery of qubits has been made based on intuition; however, conducting experimental tests on these circuits is financially impractical because of the wide range of variations in each element's values and circuit layouts. Fortunately, sufficient qubits are available to comprehend their quantum properties and optimize their Hamiltonians. This realization leads to developing a tailored optimization approach that can work optimal values out of general circuits to provide direction and solution in a search for long coherence time in qubits. Hence, the development of the "Numerical Optimization of Superconducting Circuits" project has evolved to explore qubits beyond known circuit design and tested them to find qubits with longer coherence times, as shown in Figure 2. The software, Scoptimization (see more details in Section 5), is assigned to examine and identify optimal qubits based on provided general circuit configurations. The project infrastructure is a build-up package to a project and a Python software known as Scqubits (see more details in 5.1), facilitating the initialization of circuit elements and noise parameter analysis, along with additional information for further manipulations. Within the Scoptimization framework, the focus lies on developing a generalized cost function that can accommodate diverse circuit configurations without needing prior knowledge of individual qubits. The software is currently in a testing phase, where it has been evaluated using known qubits such as Transmon (see more details in Section 6.1) and Fluxonium (see more details in Section 6.2). This evaluation aims to assess its ability to identify optimal values for the circuit Hamiltonian and match it with experimentally validated values. Thus, there is a potential search engine for general superconducting circuits.

Chapter 1

Circuit components

The superconducting circuits are constructed using various components that play a distinctive role in achieving atom-like behavior. Hence, there is a primary focus on three critical electrical elements crucial for the alignment of fully functional qubits: linear capacitors, linear inductors, and non-linear Josephson junctions; their circuit symbols are shown in Figure 1.1.

Figure 1.1: Three circuit elements. (a) Circuit symbolism for a linear capacitor - C. (b) Circuit symbolism for a linear inductor - L. (c) Circuit symbolism for a non-linear Josephson junction - E_J and C_J.

To comprehensively analyze the circuit, it is crucial to investigate the mathematical calculations to determine the system's total energy, preferred as Hamiltonian in quantum physics. Defining the system's equations of motion is imperative in studying circuits, typically relating voltage and currents across various components [10]. These components feature two connection points within a branch, enabling current flow. Fundamentally, the component can be defined by two variables simultaneously: the voltage traversing across it and the current passing through the circuit, with opposite orientations. This current and voltage behavior can be explained by an underlying electromagnetic field, described by Maxwell's equations [10]. Fortunately, the calculations are simplified by assuming the fields are well outside the components. Additionally, defining variables like flux and charge, which can relate to voltage and current, is possible due to Kirchhoff's laws. This process helps define accumulated charge at a node and external magnetic flux through a loop [10]. Ultimately, this facilitates the translation of circuits into graph theory. This specific mathematical approach converts the circuit into nodes and branches, which serve as the foundation for deriving capacitors' energy and inductors later in the following two sections.

1.1 Linear elements - capacitor and inductor

1.1.1 Capacitor

A linear capacitor, whose circuit representation is shown in Figure 1.1(a), functions as a device for storing electrical energy through the accumulation of electric charges on two closely positioned conducting plates separated by insulated material. After the voltage is applied across those plates, an electric field between them is created due to the accumulation of electric charge on the plates. The role of insulation between the plates is to create a carrier that prevents current from flowing through. The storage capacity of the capacitor is defined as capacitance [11]. The equation describing the total energy of the capacitor is formulated in terms of magnetic flux and is given by:

$$E = \frac{1}{2} C \dot{\Phi}^2, \tag{1.1}$$

where C represents its capacitance and Φ denotes magnetic flux. Further derivation and details about this equation can be found in [10]. Eq. (1.1) is crucial for applications in the Hamiltonian for superconducting circuits as it directly influences the energy state of qubits. This energy parameter will be a key focus for optimization using Scoptimization to improve coherence time by reducing charge noise (see more in Section 3.2.1 about charge noise).

1.1.2 Inductor

A linear inductor, as illustrated in Figure 1.1(b), constitutes an essential component within circuits, physically manifesting as a coil of wire through which electrical current flows, generating a magnetic field around it. Similarly to capacitors and their relationship with voltage, the intensity of the magnetic field produced by the current is directly proportional to the inductance. The primary function of an inductor lies in its ability to resist changes in the flow of current. Whenever the current through an inductor undergoes alteration, the corresponding magnetic field also adjusts, thereby inducing a voltage that opposes the change in current. Remarkably, an inductor can store energy within its magnetic field as current flows through it. In alternating current circuits, inductors introduce impedance to the current flow, a characteristic known as inductive reactance, which exhibits variation in response to frequency changes [12]. The resulting equation for the total energy of the inductor is formulated in terms of magnetic flux and is given by:

$$E = \frac{1}{2L} \Phi^2, \tag{1.2}$$

where L represents its inductance and Φ denotes magnetic flux. Additional derivations and detailed explanations of this equation are available in [10]. Eq. (1.2) is relevant in superconducting circuit Hamiltonians, as it directly influences qubit potential energy and well shape. When an inductor forms a closed loop with another linear or nonlinear inductor (Josephson junction), it generates an external magnetic flux crucial for manipulating circuit Hamiltonian energy parameters, a topic explored further in subsequent chapters. The optimization of this energy parameter will be a primary focus, using optimization techniques to enhance coherence times.

1.2 Non-linear element - Josephson junction

Josephson junction emerges as the most pivotal element within the circuit. This recognition is primarily attributed to its non-linear properties, resulting from using superconducting material in its construction [13]. Its role is to transform a circuit into an artificial atom, thereby facilitating the creation of a qubit. Its circuit symbolism is found in Figure 1.1(c).

1.2.1 Josephson junction and superconductivity

To understand the Josephson junction and its leading role in superconducting circuits, it is crucial to comprehend superconductivity, including its underlying causes and remarkable properties or phenomena. Superconducting materials exhibit unique properties when cooled below their critical temperature, resulting in phenomena such as the Meissner effect and the BCS Theory, demonstrated by zero resistance and the expulsion of magnetic fields.

The BCS theory describes electrons near the Fermi level in a material, forming Cooper pairs. This pairing arises from electron interaction within the material's crystal lattice, facilitated by lattice vibrations or phonons. These phonons induce a subtle attraction between electrons, resulting in Cooper pairs with opposite momentum and spin, bound together by interaction with lattice vibrations. [14]. This cooperative behavior among electrons, mediated by phonon interactions, is crucial for understanding the emergence of superconductivity in specific materials and concluding in zero resistance that will have an across-the-junction supercurrent.

The Josephson junction's design compromises two superconductors separated by a thin resistive barrier shown in Figure 1.2. The purpose of the barrier is to block electrons during classical conditions. When a direct current is applied to the junction, the Josephson effect typically results in zero current. This phenomenon demonstrates the quantization of magnetic flux, indicating that the magnetic flux passing through a superconducting loop is quantized in multiples of the flux quantum. This quantization permits discrete quantities of magnetic flux to be confined within the loop, forming persistent circulating currents. Supercurrent, the flow of electrical current without resistance through the junction when biased below a critical current, arises from the coherent quantum tunneling of Cooper pairs of electrons across the insulating barrier. An increment in the applied current results in the supercurrent flowing through the junction and hitting the critical value of the junction [16].

While the voltage remains zero across the junction, upon surpassing the critical value, it transitions into a resistive state characterized by tunneling individual electrons through the barrier, resulting in a finite voltage drop across the junction [17]. The Josephson equations describe the behavior of the Josephson junction:

$$I = I_0 \sin(\varphi), \tag{1.3}$$

where I is a supercurrent flowing through the junction to the phase difference $\varphi = (\varphi_1 - \varphi_2)$ between the wave functions of Cooper pairs in the two superconductors, while I_0 describes the critical current of the junction [13]. When a constant voltage is applied across the junction, the Eq. (1.3) predicts an oscillating current at a nonzero voltage.

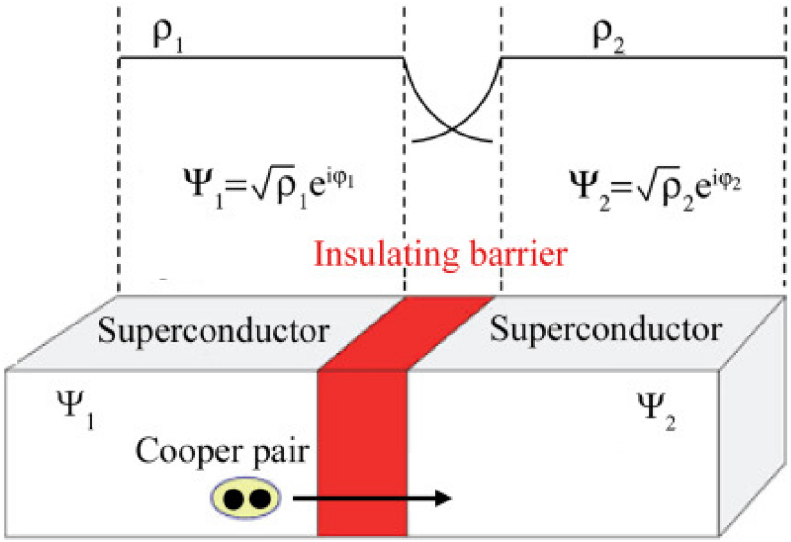

Figure 1.2: The non-linear Josephson junction comprises two parts made of superconducting material, separated by an extremely thin insulating barrier. Here, Cooper pairs of electrons can tunnel through the junction. An exponential wavefunction characterizes each Cooper pair. In the DC Josephson effect, when no voltage is applied, a current proportional to the phase difference of the wavefunctions can flow through the junction. In the AC Josephson effect, the junction oscillates at a frequency relative to the voltage. When no current is applied, a single wavefunction can describe all Cooper pairs in a superconductor, as they share the same phase, resulting in phase coherence. The wavefunctions of Cooper pairs on each side of the junction penetrate the insulating region and synchronize in phase, allowing current flow without applied voltage (the DC Josephson effect) [13]. Image taken from [15].

Further, the critical current I_0 can be characterized by Josephson energy, linked to Cooper pair tunneling [14]. By applying Eq. (1.3) and utilizing $V = LdI/dt$ to characterize the inductance of the Josephson junction, it is possible to recognize that this results in a nonlinear element due to the cosine term. This results in the total energy of the Josephson junction expressed as:

$$PE = -E_J \cos(\varphi), \tag{1.4}$$

where the energy is described by $E_J = I_c\Phi_0/2\pi$ [13]. The parameter E_J plays a significant role in the optimization part of this project, as it is crucial in determining the value that will yield the best results for the designed circuit. Detailed calculations and explanations can be found in [13].

Chapter 2

Quantum harmonic oscillator and LC circuit

The connection between the Quantum Harmonic Oscillator (QHO) and its wavefunction representation is denoted in Figure 2.2, and LC circuits, displayed in Figure 2.1, stem from their analogous behavior, both characterized by harmonic oscillations in energy states. This analogy establishes a mathematical framework, allowing us to derive a Hamiltonian that describes the dynamics of these systems in quantum terms. The QHO exhibits a profound relationship with a capacitor and inductor that are parallel connected, forming an LC circuit.

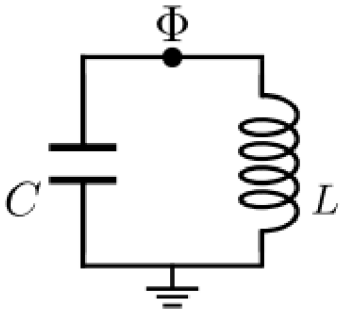

Figure 2.1: The LC circuit represents the most basic circuit form, where a harmonic oscillator can be applied to superconducting circuits. In this setup, electrical energy oscillates between the kinetic energy stored in the capacitor C and the potential energy associated with the magnetic flux in the coil Φ [18]. Image taken from [18].

Introducing the QHO Hamiltonian:

$$\hat{H} = \frac{\hat{p}^2}{2m} + \frac{m\omega^2\hat{x}^2}{2}, \tag{2.1}$$

where the kinetic energy component is described by the mass of the particle m and $\hat{p}$, the momentum operator of the system, while the potential energy is determined by the mass m, angular frequency ω of the oscillator, and the position operator $\hat{x}$ [20].

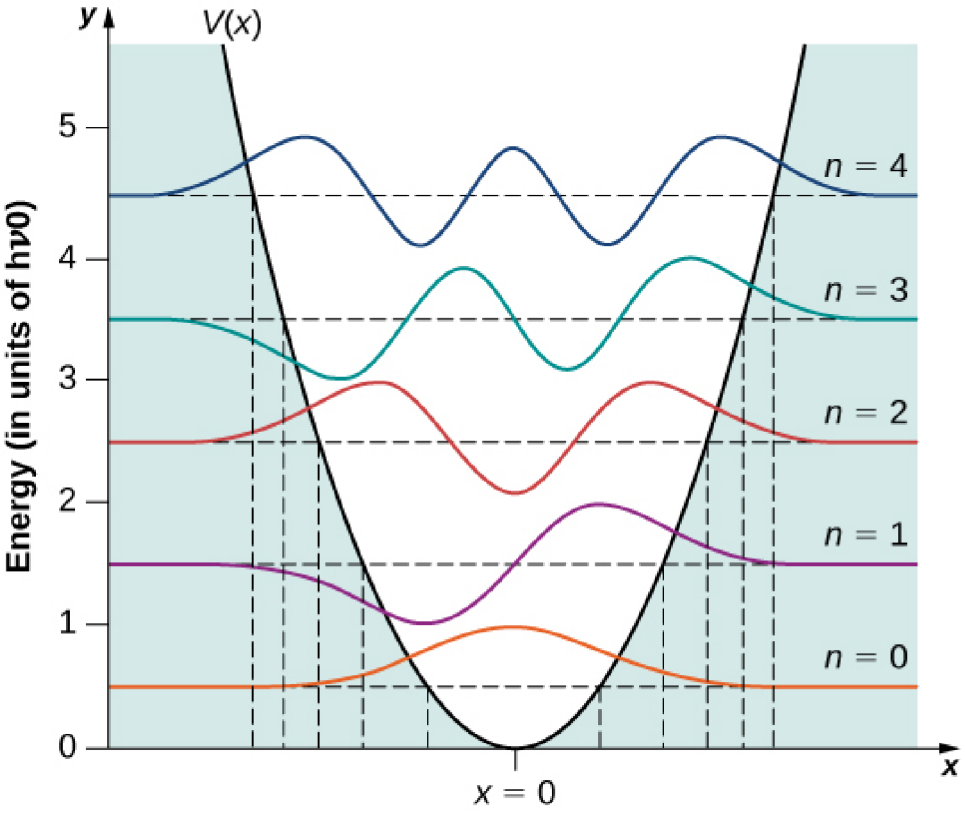

Figure 2.2: The Quantum Harmonic Oscillator (QHO) typically features a parabolic potential well, representing the potential energy of the oscillating particle. Within this well, discrete energy levels are depicted as horizontal lines, showcasing the quantized nature of the oscillator's energy states. Wavefunctions overlay each energy level, depicting the probability distributions of finding the particle at different positions within the well. The ground state wavefunction, corresponding to the lowest energy level, often exhibits a single peak centered around the oscillator's equilibrium position. As energy levels rise, wavefunctions become more intricate, with multiple peaks indicating areas of higher probability density. The horizontal axis represents the particle's position within the well, while the vertical axis represents the amplitude or probability density of the wavefunction at each position. This visualization provides insight into the spatial distribution of the particle's probability density as it oscillates within the potential well, encapsulating the essence of the quantum harmonic oscillator's behavior [19]. Image taken from [19].

This dynamic interplay between kinetic energy (mass) and potential energy (position operator) can be correlated with the parameters of the LC circuit. By summing the total energies of a capacitor and an inductor, expressed in Eqs. (1.1) and (1.2) respectively, and applying the Lagrangian framework, where Eq. (1.1) represents the kinetic part and Eq. (1.2) represents the potential part, a Legendre transformation can be applied. This transformation involves calculating the momentum conjugate to the flux, resulting in the Hamiltonian for the LC circuit:

$$H = \frac{Q^2}{2C} + \frac{\Phi^2}{2L}, \tag{2.2}$$

where Q represents the charge on the capacitor with capacitance C, Φ denotes the magnetic flux threading the inductor with inductance L. For detailed calculations of the Hamiltonian in 2.2, refer to [17]. By comparing the two Hamiltonians above, it becomes evident that the mass is analogous to the capacitance, and the position operator represents the flux. However, this comparison only establishes a relationship between them. The Hamiltonian in Eq. (2.2) is classical, and its charge and flux coordinates must be transformed into quantum operators. This transformation involves applying commutation relations and replacing the charge and flux with their respective quantum operators, resulting in Hamiltonian suitable for the optimization application [18]. Its form is displayed as follows:

$$\hat{H} = 4E_C\hat{n}^2 + \frac{1}{2}E_L\hat{\phi}^2, \tag{2.3}$$

where it incorporates the charging energy parameter $E_C = e^2/(2C_\sum)$, $C_\sum = C_s + ...$, where $C_\sum$ is the capacitance of the system, initially determined solely by the capacitor until Josephson junctions are added or another capacitor. The E_C represents the energy required to add each electron of the Cooper pair to the island, thus involving reduced charge, $\hat{n} = Q/2e$. Additionally, inductive energy E_L is defined as $E_L = (\Phi_0/2\pi)^2/L$, incorporating the superconducting magnetic flux quantum $\Phi_0 = h/(2e)$, where the Eq. (2.3) with more detailed explanation can be found in [8]. The Hamiltonian in 2.3, comprising its kinetic and energy components, will drive the optimization process. Subsequently, we will explore how the kinetic part shapes energy levels and how the potential part defines the qubit's potential well.

Chapter 3

Noise and decoherence

The fundamental principle is that solid and well-functioning quantum computers must be made of qubits with decent stability and long coherence time. So far, the superconducting circuit has been discussed only as a perfectly closed system. Unfortunately, realistically, external factors hinder the quantum system and affect the Hamiltonian. Hence, the interactions between the circuit environment and the external environment influence a challenge to the qubit's lifetime. Multiple noises have an impact on these systems and their performance. Figure 3.1 illustrates how variations in circuit input values correspond to changes in noise levels. Various approaches can mitigate noise and enhance qubit efficiency, including advancements in materials science, fabrication technology, electronics design, and cryogenic engineering [21]. However, the project also involves an alternative approach: designing the circuit's layout. It is possible to engineer qubits to be less susceptible to specific types of noise while improving sensitivity to others.

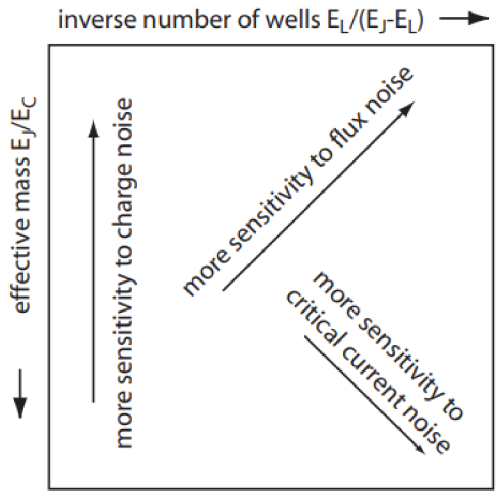

Figure 3.1: The graph illustrates the delicate equilibrium between the Hamiltonian energy parameters of a circuit and their relationship with various sources of noise that induce decoherence. For instance, a low ratio of the Josephson energy parameter (E_J) to the charging energy parameter (E_C) leads to high charge noise. Image taken from [22].

3.1 Types of noise

3.1.1 Systematic noise

Systematic noise is the type of noise that is consistent and reproducible, arising from inaccuracies in control and readout processes. For instance, miscalibration when sending pulses to a qubit can result in over-rotation or under-rotation. These errors, often found in machinery, experimental setups, and application patterns, can be mitigated by adjusting calibration procedures or improving hardware design [8]. This noise can be mitigated by utilizing different layouts of circuit elements and adapting the circuit Hamiltonian to enhance protection.

3.1.2 Stochastic noise

Stochastic noise, arising from environmental fluctuations beyond control, is a random disturbance impacting quantum systems. Major sources include thermal fluctuations like Johnson noise and fluctuating electromagnetic fields surrounding qubits, leading to quantum information loss known as decoherence. This noise, stemming from variables such as voltage and current fluctuations, poses challenges due to its unpredictable nature [8]. This type of noise can be reduced by precise setup and proper machinery, along with adjustments to the circuit and engineering to enhance precision.

3.2 Examples of noise

Introduction to a couple of different types of noise that need to be addressed during circuit layout manipulation. Understanding how these noise factors affect the circuit improves coherence time and stability during readout processes.

3.2.1 Charge noise

Charge noise occurs due to fluctuations in the local electric field caused by random trapping and de-trapping of charge carriers in defects near qubits. This specific noise affects those qubits with circuits that rely on electrostatic gates, like charge qubits. These fluctuations in electric fields can unpredictably manipulate the energy levels of the qubits [22]. Strategies to mitigate charge noise in superconducting circuits include using materials with low trap densities, optimizing electrode design to minimize charge trapping, and incorporating circuit designs that are less susceptible to charge fluctuations. Isolation techniques can shield the circuit from external noise, while dynamic error suppression methods and feedback control systems further enhance performance and stability.

3.2.2 Magnetic flux noise

Magnetic flux noise or flux noise emerges from the fluctuations in the magnetic environment surrounding superconducting circuits. This noise results from different sources, including spins on material surfaces and imperfections in the superconducting materials. Flux noise produces the same effect as charge noise, which shifts between energy levels of qubits, but it explicitly affects those designed to be sensitive to magnetic flux, such as

the Flux qubit. Scientists are still studying ways to reduce flux noise, aiming to understand its origins and find solutions to eliminate it [22]. Strategies to reduce flux noise in superconducting circuits include using high-purity materials, shielding against external magnetic fields, and operating at low temperatures. Techniques such as flux tuning, dynamic decoupling, and feedback control also help mitigate noise effects, enhancing circuit performance and stability.

3.3 Models of noise in Bloch sphere

The Bloch Sphere visually represents the qubit's state, where the ground and the first excited states are found along the z-axis. At the same time, any other point in space represents a superposition of these states. The impact of noise can be described as a movement of its state point away from the intended location on the Bloch sphere, indicating decoherence or state transitions induced by noise. These external influences impact qubit stability, altering its position on the Bloch sphere and transitioning it from its natural state to the ground state [10].

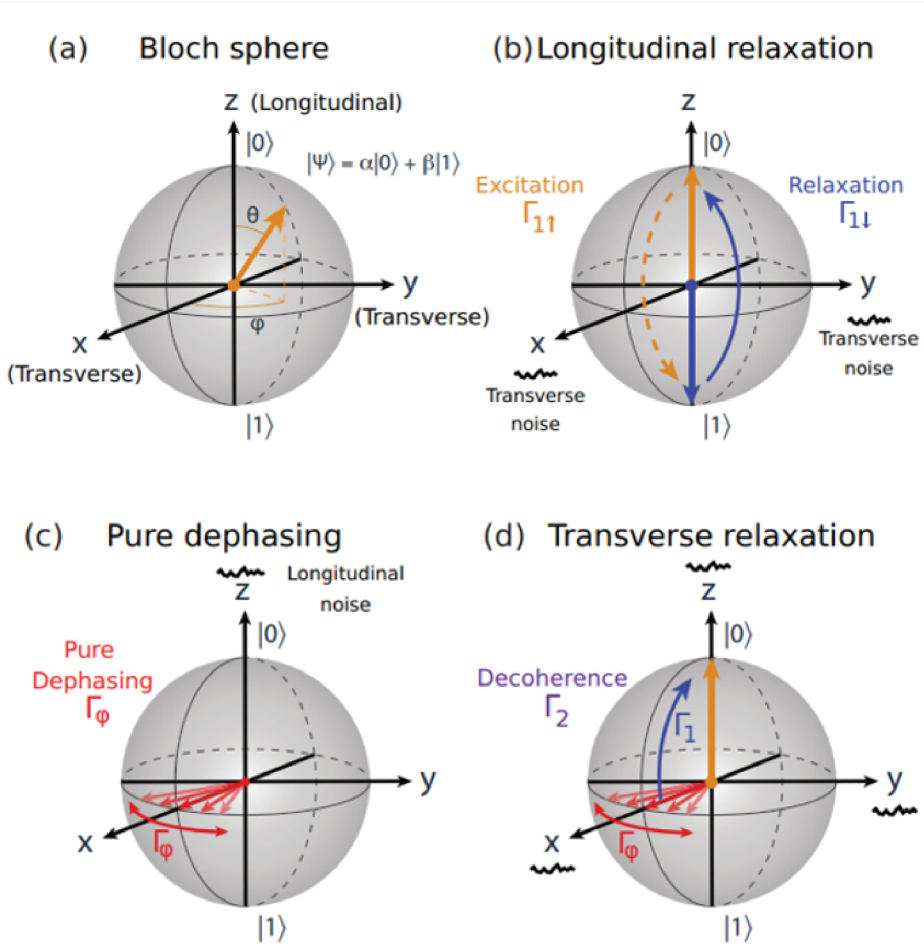

Figure 3.2: Bloch sphere presentation of transverse and longitudinal noise. (a) An arbitrary quantum state of the qubit is represented on the Bloch sphere, where the z-axis signifies longitudinal direction, and the x-y plane denotes transverse orientation. (b) The longitudinal relaxation rate indicates how quickly a qubit state returns to its equilibrium state after excitation. The reciprocal of the longitudinal relaxation time T_1 defines the timescale over which a qubit in an excited state loses energy to its surroundings and returns to a lower energy state, which is affected by transverse noise. A blue arrow represents a qubit transitioning to its ground state denoted as $\Gamma_{1\downarrow}$, while a qubit absorbing energy from its environment and reaching the first excited state is indicated by an orange arrow denoted as $\Gamma_{1\uparrow}$. (c) Pure dephasing rate, symbolized as Γ_{φ}, occurs when a qubit loses phase coherence without exchanging energy with the environment, which affects the relative phase between its ground state and excited state. Transverse pure dephasing originates from longitudinal noise along the z-axis, inducing fluctuations in the qubit frequency. As a result of these stochastic frequency variations, a Bloch vector positioned along the x-axis undergoes diffusion, rotating either clockwise or counterclockwise around the equator. This process leads to the depolarization of the azimuthal phase at a certain rate. (d) Transverse relaxation rate, denoted as Γ_2, describes the decay of a qubit's phase coherence. This relaxation is influenced by pure dephasing and energy exchange with the environment [8]. Image taken and adjusted from [8].

3.3.1 Longitudinal relaxation - T_1

The longitudinal relaxation rate, denoted by Γ_1, represents energy decay along the z-axis, influenced by transverse noise. Depolarization occurs due to energy exchange between the system and its external environment, leading to qubit excitation and relaxation. The Γ_1 plays a significant role in its direct correlation with the ability of a qubit to retain information. If the Γ_1 time is too short, the qubit will revert to its ground state too quickly, limiting the time to perform any computations [10]. Figure 3.2(a) shows the concept of this effect on the qubit. However, improving Γ_1 presents a significant challenge, yet addressing noise can be achieved by selecting superior materials, utilizing advanced engineering techniques, and emphasizing circuit design enhancement within this project.

3.3.2 Pure dephasing - T_ϕ

Pure dephasing, denoted as T_ϕ, describes the loss of phase coherence in a qubit without energy exchange with the environment. Although the qubit's state population remains unchanged, the relative phase information between states is lost [10]. Visualized on a Bloch sphere in Figure 3.2, pure dephasing occurs on the x-y plane, causing the qubit's representation to shrink toward the axis. This shortens the vector's length without moving it closer to either pole, diminishing the quality of the qubit's superposition, which is crucial for quantum algorithms—symbolized as Γ_Φ, it represents the timescale over which phase coherence is expected to dissipate. In superconducting qubits, various noise types like 1/f noise or charge fluctuations can induce pure dephasing, erratically altering the qubit's phase without correlation to energy eigenstate populations [10].

3.3.3 Transverse relaxation - T_2

The transverse relaxation rate, Γ_2, encompasses both energy relaxation (Γ_1) and pure dephasing (Γ_Φ), defining the duration a superconducting qubit can maintain coherence in its quantum superposition states, such as $|0\rangle$ and $|1\rangle$. During this time, the qubit's phase relationship remains crucial for quantum operations reliant on interference patterns. However, noise from various sources can induce state dephasing, compromising coherence. For instance, fluctuating magnetic fields can alter the qubit's energy levels, accelerating coherence loss beyond Γ_1's expectations. Hence, T_2, a transverse relaxation time, is a comprehensive measure of overall coherence amidst environmental interactions [10]. Maximizing T_2 is a primary project goal, achieved through optimization methods and exploring diverse circuit layouts to extend coherence duration, directly impacting computational power and reliability by determining the number of feasible quantum operations within coherence time. This impact is illustrated on the Bloch sphere in Figure 3.2(c), showcasing how Γ_2 combines pure dephasing and longitudinal relaxation rate.

$$\Gamma_2 = \frac{1}{T_2} = \frac{\Gamma_1}{2} + \Gamma_\varphi \tag{3.1}$$

Chapter 4

Types of qubits

4.1 Cooper-pair box - CPB

The Cooper-pair box (CPB) is a predecessor qubit design comprising a superconducting circuit with a Josephson junction. This configuration introduces nonlinearity, resulting in anharmonicity and establishing a two-level system. Additionally, the circuit includes a voltage source capacitively coupled to the superconducting island, enabling control over the CPB's operating point. Adjusting this voltage allows manipulation of the number of Cooper pairs on the island, facilitating state initialization for experimental purposes. Mathematically, the behavior of the CPB can be described by a Hamiltonian:

$$\hat{H} = 4E_C\hat{n}^2 - E_J \cos\hat{\varphi}, \tag{4.1}$$

where the system's energy is based on the number of tunneled Cooper pairs ($\hat{n}$), with the addition of the offset charge (n_g), and the phase difference across the Josephson junction ($\hat{\varphi}$), the E_C represents charging energy in the system, and E_J represents the Josephson energy.

The state of the CPB can be controlled by adjusting the offset charge n_g using an externally applied voltage. Ideal computational manipulation occurs when n_g reaches an optimal value, either an integer or a half-integer. Additionally, n_g directly influences the qubit's operating frequency ω_q, which depends on the energy gap between its levels, dictating the microwave frequencies it can absorb or emit [23]. Configuring the CPB to operate at specific points where this energy difference enables precise transitions between states is crucial. While integer values of n_g are essential for initializing the CPB to its ground state, half-integer values prove more effective for qubit operations due to enhanced separation between energy levels of the first two excited states, as illustrated in Figure 4.1.

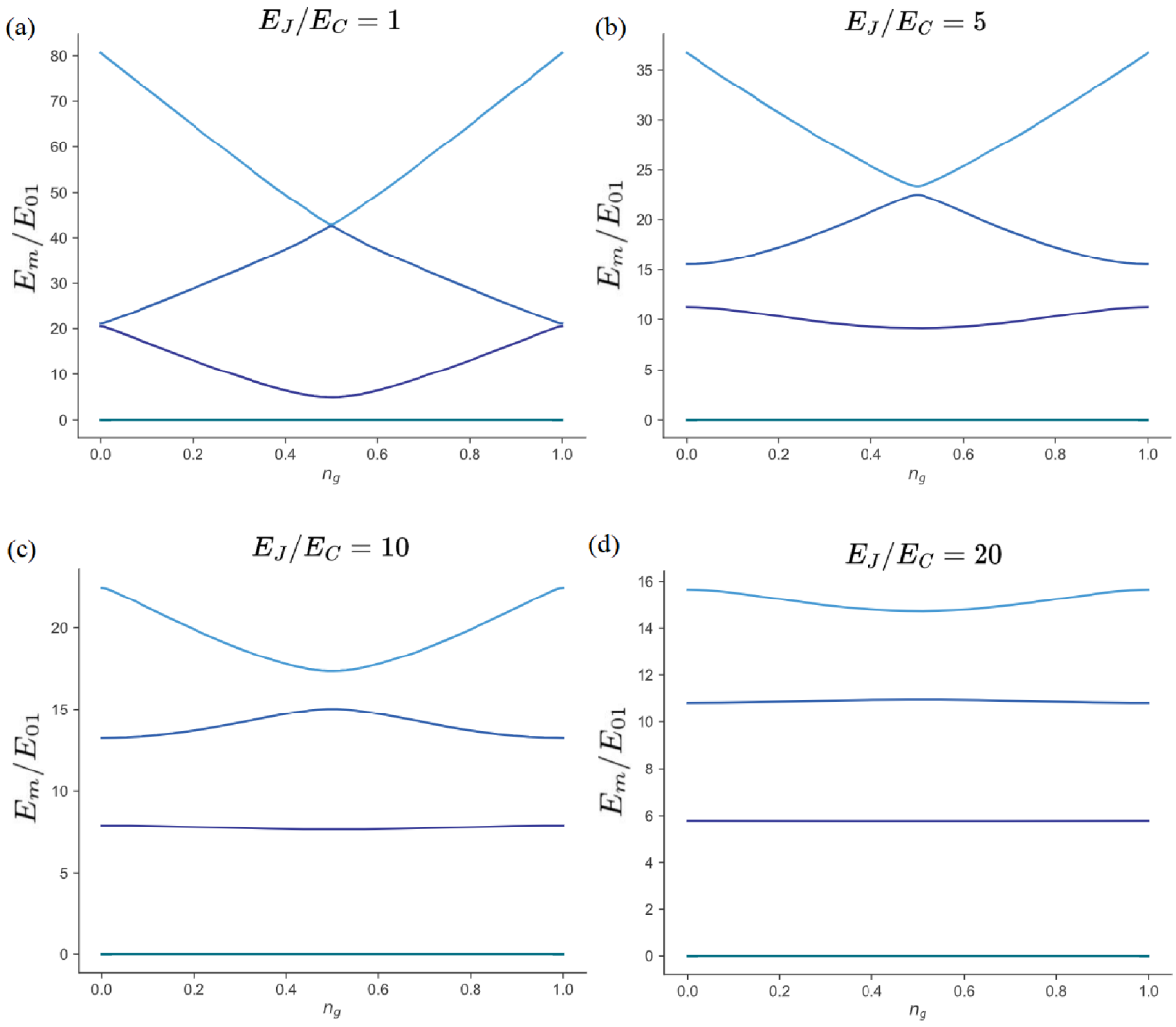

Figure 4.1: The anharmonicity at low energy ratios, with an increase in the ratio leading to harmonicity in the Cooper Pair Box (CPB). The eigenenergies (E_m) represent the first four levels (m=0,1,2,3) of the qubit Hamiltonian Eq. (4.1) as a function of the effective offset charge (n_g) for different ratios (E_J/E_C). In (a), the ideal spot at $n_g = 0.5$ exhibits the best anharmonicity among all levels in the CPB regime [23]. However, in (b), (c), and (d), there is a decrease in anharmonicity alongside an exponential increase in charging noise [24]. The (c) and (d) graphs are represented in the Transmon regime, which is discussed in the following section. However, finding optimal values for the energy parameters is essential to achieve good anharmonicity and noise reduction for high coherence time. Image taken and adjusted from [23]. Plots created by Scqubits Python package.

Figure 4.1(a) at these half-integer points, energy levels demonstrate anharmonicity, which enables selective driving of transitions between ground and first excited states, reducing the risk of unintended higher-energy state transitions—essential for operational qubit control. Resonant excitation, achieved by applying microwave pulses corresponding to the energy difference between desired states, enables specific and controlled transitions without affecting other states. In Figure 4.1(d), the energy level's stability near $n_g = 0.5$ reduces sensitivity to offset charge changes, improving coherence times (T_2) needed for maintaining quantum states against external disturbances like charge noise. Longer coherence times support complex quantum processes with sequential gates, allowing extended computation without losing quantum information. Anharmonicity at $n_g = 0.5$ is crucial for precise qubit control, forming the basis of CPB qubit operations by creating a reliable energy landscape for efficient quantum computing. This stability protects against errors and enables smooth manipulation, vital for gate implementation and operational versatility [23].

On the other hand, the coherence time for CPB needs to be increased to use this qubit and apply gates to it. It is enormously influenced by charge noise caused by the gate voltage fluctuations. A capacitor is introduced into the circuit to address this issue, giving rise to a new type of qubit known as Transmon.

4.2 Transmon

The Transmon qubit, derived from the CPB architecture, stands out as one of the most prominent qubit designs for extending coherence time. Its conceptual enhancement involves introducing a significant shunted capacitance (C) in conjunction with the Josephson junction, a strategy devised to mitigate the impact of voltage gate imperfections inherent in superconducting circuit designs as illustrated in Figure 4.2.

The modification has minimal impact on the circuit system's Hamiltonian, which is

$$\hat{H} = 4E_C(\hat{n} - n_g)^2 - E_J \cos\hat{\varphi}. \tag{4.2}$$

It is the same as the CPB Hamiltonian shown in Eq. (4.1). It differed with the added shunted capacitance to the total charging energy in the system, $E_C = e^2/(2C_\sum)$, $C_\sum = C_g + C_J + C$, where $C_\sum$ is taken from [23] and can elaborate more on the mathematical viewpoint.

One of the main characteristics of Transmon qubit lies in its E_J/E_C ratio, a parameter that can be manipulated to observe distinguishable changes in the system, whether the qubit operates within the CPB or Transmon regime. This ratio is a critical determinant of the qubit's behavior, influencing its anharmonicity—a crucial aspect governing its ability to maintain superposition and transition between energy levels. A comprehensive analysis of these regimes, as portrayed in Figure 4.1, underscores how variations in the E_J/E_C ratio directly impact the qubit's anharmonicity profile and insensitivity to charge noise. In the Transmon regime, characterized by $E_J/E_C >> 1$ or in Figure 4.1(d), the qubit exhibits reduced anharmonicity algebraically. However, it results in an exponential decrease in charge dispersion, increasing Transmon's lifetime, as presented in Figure 2.

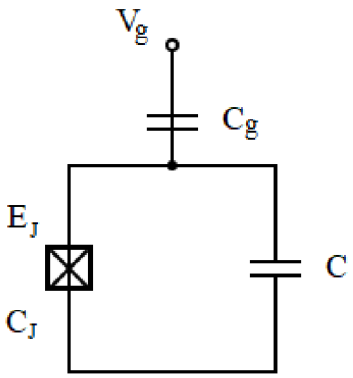

Figure 4.2: Transmon qubit - superconducting circuits design. The total energy of the Josephson junction is noted as E_J, and the capacitance of the Josephson junction C_J, along with the gate capacitance C_g contribute collectively to the overall capacitance of the system. However, the most significant capacitance C acts as a shunted capacitance, playing a key role in reducing the total charging energy, which is determined by: $E_C = e^2/(2C_\sum)$, where $C_\sum$is the total capacitance of the qubit island. The importance of C lies in its impact on the ratio E_J/E_C. By driving the capacitance C to sufficiently high values, such that $E_J/E_C >> 1$, the resulting ratio places the system in the Transmon regime. This characteristic is crucial for reducing charging noise, consequently extending the coherence time of the system [23]. Image taken and adjusted from [23].

4.2.1 Transmon's Hamiltonian - parameters and their functions

Transmon's Hamiltonian in Eq. (4.2) significantly affects the energy levels and the potential well compared to the one for the quantum harmonic oscillator, presented in Figure 2.2, due to the presence of the Josephson junction, introducing nonlinearity and enabling the idea of the two-level system. Compared to the harmonic oscillator's potential energy, which is quadratic, Transmon's Hamiltonian introduces a cosine term, inducing anharmonicity.

The behavior of the Transmon can be explored by varying the Josephson energy E_J and charging energy E_C ratios. Figure 4.3 depicts different Transmon ratio configurations, illustrating plotted wavefunctions of energy versus phase. In Figure 4.3(a), Transmon representation with $E_J = 7$ GHz and $E_C = 0.2$ GHz is portrayed with a ratio $= 35$, where it is insensitivity to charging noise, leading to increased coherence times. In Figure 4.3(b), the display illustrates the impact of setting the Josephson energy to $E_J = 12$ GHz. This change causes the height of the well to increase, indicating that the E_J term acts as an amplitude, altering the boundaries of the well. The energy levels will also space out. Figure 4.3(c) displays the effect of decreasing the total charging energy to $E_C = 0.2$ GHz, achieved by increasing the shunted capacitance. This implies that the energy levels become closer together. It can be likened to mass: a larger capacitance makes the system "heavier" and causes it to drop deeper into the potential well. The observation of the well indicates that higher ratios tend to result in a harmonic potential shape. On the other hand, reducing the ratio by increasing the charging energy to $E_C = 2.05$ GHz while keeping E_J constant yields a noticeable change, as depicted in Figure 4.3(d). Here, the energy levels become more spaced out, and notably, the first excited

state is positioned outside the potential well. This observation is crucial for assessing the boundedness of the qubit, as discussed further in Section 5.

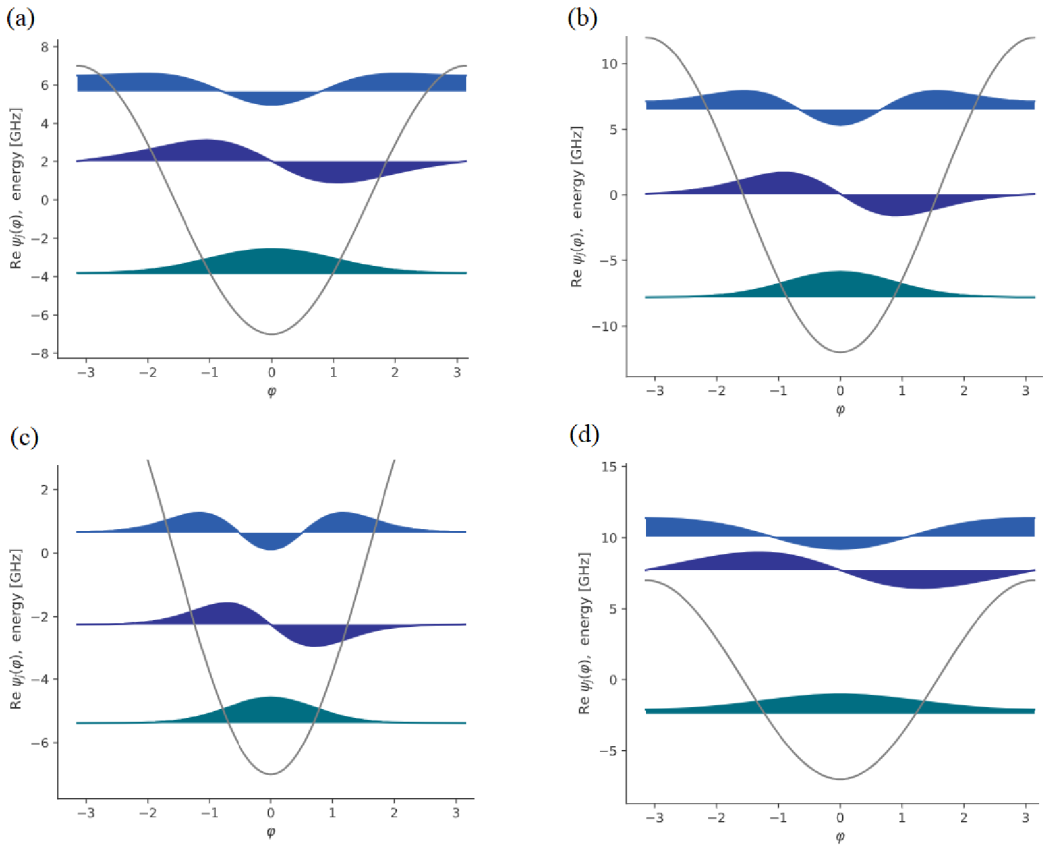

Figure 4.3: Transmon wavefunction representation and ratio explanation (units = GHz). (a) The Transmon is set to $E_J = 7$ GHz $E_C = 0.2$ GHz, which results in ratio $E_J/E_C = 35$ (b) Transmon qubit, where Josephson energy is set to $E_J = 12$ GHz and charging energy to $E_C = 1.0$ GHz. (c) Transmon where the Josephson energy stays the same as in (b), and it adjusts the charging energy to $E_C = 0.2$ GHz, making the energy levels closer together and dropper lower in the cosine well. (d) In the case of the Transmon, adjusting the charging energy to $E_C = 2.05$ GHz leads to a decrease in the ratio, causing the energy levels to become more spaced out. Consequently, the first excited state is positioned outside of the potential well. Plots created by Scqubits Python package.

4.3 Fluxonium

Fluxonium is a type of flux qubit found in superconducting circuits, where quantum information is stored in magnetic flux states. These qubits are fabricated of loops of superconducting material with one or more Josephson junctions. The direction of the supercurrent in the loop determines the qubit states, reflecting different magnetic flux quantum states. Adjusting the external magnetic flux passing through the loop allows the qubit's states to be controlled and tuned. One key advantage of flux qubits is their relative insensitivity to electric field noise because their energy states are based on current and magnetic fields rather than electric charges. However, they can be sensitive to flux noise and require careful shielding [25]. The circuit design of the qubit is in Figure 4.4, where a new parameter, the "linear" inductor, has been incorporated. This linear inductor comprises an array of multiple Josephson junctions interconnected, often referred to as a superinductance[26].

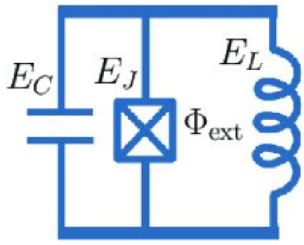

Figure 4.4: Fluxonium circuit design - E_C represents a charging energy, E_J is a Josephson junction energy, and E_L is an inductive energy given by $E_L = (\hbar/2e)^2/L$. Due to the Josephson junction and inductor, it will create external magnetic flux denoted by Φ_{ext}. Image is taken from [27].

One characteristic that sets Fluxonium apart from other qubits is the condition $E_L << E_J$, indicating that the behavior of the system is predominantly governed by the Josephson junctions rather than the inductive elements. Additionally, a significant ratio between the Josephson energy and charging energy, typically adjusted to $1 \leq E_J/E_C \leq 10$, helps define the operating regime of the Fluxonium qubit. Meeting these conditions necessitates a substantial inductance, often achieved by incorporating around 100 Josephson junctions into the design [28]. The kinetic inductance of this chain of junctions adds up to provide the necessary total inductance (L). The kinetic inductance is due to the inertia of the Cooper pairs (the pairs of electrons that carry the supercurrent) moving through the Josephson junctions. [29] The weak junction is effectively short-circuited at low frequencies, meaning the qubit is not sensitive to offset charges. This is beneficial because offset charges can introduce noise and errors. Unlike other qubit designs that might require large shunting capacitances to decrease sensitivity to charge noise, the Fluxonium design does not, which allows for greater circuit anharmonicity [28]. Using a chain of nearly 100 Josephson junctions, the Fluxonium qubit design effectively suppresses flux noise. This suppression is critical because flux noise can harm the qubit's coherence and performance. Despite this suppression, the design also allows for significant frequency tuning of the qubit without significantly impacting the coherence times, which is desirable for qubit control and manipulation [28].

The Fluxonium Hamiltonian is

$$\hat{H} = 4E_C\hat{n}^2 - E_J\cos(\hat{\varphi} - \Phi_{ext}) + \frac{1}{2}E_L\hat{\varphi}^2. \tag{4.3}$$

Incorporating an additional parameter to the cosine term, the external magnetic flux Φ_{ext}, and introducing the potential energy quadratic term containing the inductive energy parameter E_L [29], alters the Hamiltonian. This addition affects both the kinetic energy, representing the total charge of the system, and the potential energy, which is influenced by E_L. Consequently, the shape of the potential well is modified, resulting in a combination of cosine and quadratic terms, as depicted in Figure 4.5. This combination can be interpreted as a cosine wave overlaid on the quadratic well.

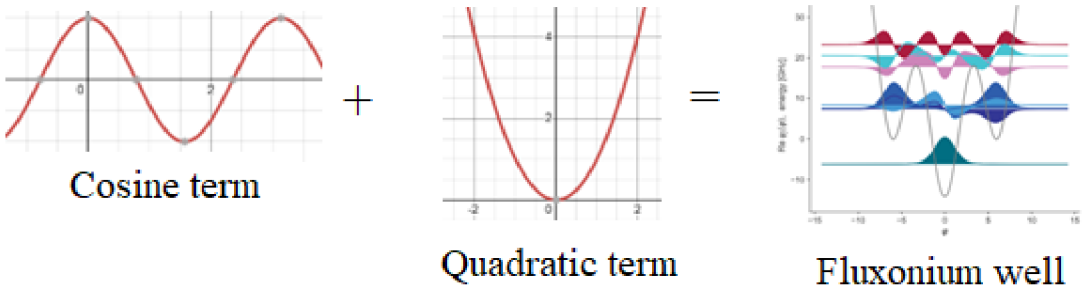

Figure 4.5: The Fluxonium's well transforms according to its potential energy and associated terms, such as cosine and quadratic components. Plots created by Scqubits Python package and Desmos.

Additionally, magnetic external flux Φ_{ext} threading the Fluxonium loop, which can be experimentally controlled. With this, there are now four parameters available for adjustment or manipulation. The variation in external magnetic flux is further explained and visualized in Figure 4.6.

In the absence of external magnetic flux (when $\Phi_{ext} = 0$), the potential exhibits three wells, as depicted in Figure 4.6(a). The central well can be regarded as the Transmon well. However, this alone does not exhaustively illustrate the uniqueness of Fluxonium. When an external flux is applied, driving it to what is termed a "sweet spot" ($\Phi_{ext} = 0.5$ or π), the potential shifts. In this regime, illustrated in Figure 4.6, the well transforms into a double well potential shape. The energy states of the qubit (ground state and first excited state) correspond to the tunneling between two potential wells that are symmetric and degenerate, meaning they have the same energy. The energy level difference produces significant anharmonicity and prolonged coherence time. This feature is particularly advantageous for handling more complex systems [10]. Additionally, driving the qubit at lower frequencies results in a natural reduction of energy relaxation (Γ_1, as processes leading to energy loss occur more slowly at lower frequencies. Consequently, the qubit can sustain its quantum state for a longer duration without necessitating improvements in the physical material of the qubit [28].

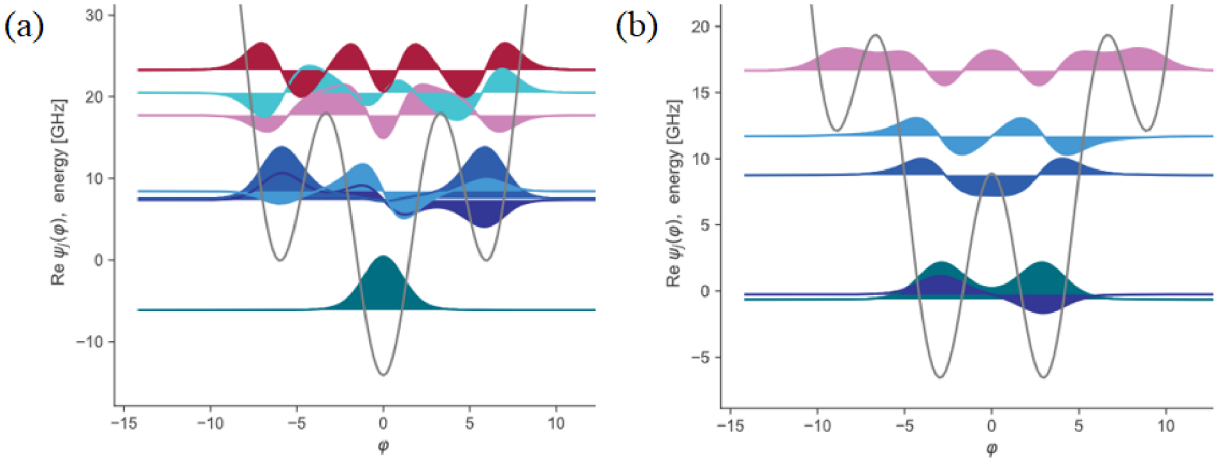

Figure 4.6: The spectrum of the Fluxonium qubit is examined under two distinct external magnetic fluxes, denoted as Φ_{ext}. (a) The Fluxonium operates with zero external magnetic flux. Here, the energy difference between its ground and first excited state corresponds to a resonant frequency akin to the plasmon frequency [28]. However, this regime does not offer any significant advantage. (b) Operating in the π regime or $\Phi_{ext} = 0.5$, the Fluxonium exhibits a double-well potential, significantly enhancing its coherence time. Plots created by Scqubits Python package.

Chapter 5

Scoptimization - numerical optimization

The "Numerical Optimization of Superconducting Circuits" project aims to develop software capable of conducting computational analysis on a broad spectrum of generic superconducting circuits. A Python package named Scoptimization has been developed, and its objective is to identify optimal values for energy parameters such as E_J, E_C, E_L, and Φ_{ext} within the given circuit. The ultimate goal is to establish an automated generation tool capable of constructing superconducting circuits with optimal coherence time based solely on provided circuit elements.

The project utilizes the Scqubits Python package, which is mentioned in the next section, along with analysis and optimization techniques to enhance the coherence time of qubits. A uniquely designed cost function aids in identifying qubits with improved coherence time. Currently, the software is undergoing development and debugging phases.

The workflow diagram of the Scoptimization software is depicted in Figure 5.1. Initially, the circuit setup incorporates elements discussed in Section 1. Subsequently, the circuit undergoes analysis of its Hamiltonian by the Scqubits Python package to define the transverse time T_2. Within Scoptimization, the analysis covers the circuit's anharmonicity and boundedness.

Figure 5.1: Framework of Scoptimization. The initial step involves configuring a circuit with predetermined elements, as Figure 1.1 illustrates. Afterward, this circuit is initialized by specifying circuit components using string type processed within the Scqubits analysis framework, where its Hamiltonian is computed. Following this computation, various parameters such as coherence time (T_2), anharmonicity (α), and boundedness (B), are determined, all of which contribute to the cost function utilized in diverse optimization methods. Finally, the exploration phase commences, allowing for comparisons between optimization methods or combining multiple methods. This process can be iterated multiple times to acquire suitable values, such as E_J, E_C, E_L, and Φ_{ext}, for the given circuit.

These qualitative and quantitative contributors play a pivotal role in constructing a comprehensive cost function, underlining the significance of your work. Qualitative contributions hinge on the value's significance, where a function is designed to decrease or increase the value compared to its previous states. On the other hand, quantitative contributions involve a step function that imposes limits irrespective of the specific value, emphasizing the necessity of staying below or above certain thresholds.

$$CF = N\left(\frac{1}{T_2}\right) + N(-\alpha) + P(B, 0) + P(\alpha, \alpha_{min}) + \dots$$

Figure 5.2: Example of a cost function featuring qualitative and quantitative contributions. The blue contribution represents the normalized reciprocal function of the coherence time T_2, a qualitative analysis. The red contribution demonstrates the normalization of a linear function with a negative slope representing the anharmonicity of the system, which also constitutes a qualitative analysis. The yellow contribution, belonging to the quantitative contribution group, signifies boundedness, penalizing values above a certain threshold (in this case, 0). The green contribution represents the critical anharmonicity, penalizing values that fall below the minimum anharmonicity of the system. This also constitutes a quantitative analysis. Adjusted from a poster for this project.

These qualitative and quantitative contributions collectively form the basis of the final cost functions, which the example of cost function is presented below in Figure 5.2. The blue segment reflects the normalized reciprocal function of the coherence time (T_2), constituting a qualitative analysis. The T_2 value is computed by using the Scqubits Python package. The red segment normalizes a linear function with a negative slope representing the system's anharmonicity (α). Anharmonicity is a value defined by Scoptimization, which compares the ground state and the first two eigenstates. This value can be both qualitative and quantitative. For qualitative analysis, the function takes a linear form with a negative slope because it is crucial for the value to be sufficiently high.

Conversely, the anharmonicity function adopts a step-like behavior for quantitative analysis, highlighted in green. It penalizes values within an acceptable range, while values falling outside this range receive higher penalties, causing the cost function to increase rapidly and render them impractical for consideration. The yellow segment, classified within the quantitative region, addresses boundedness (B), which is crucial for maintaining a two-level system, ensuring that the first excited state remains within the defined bounds of the well. As such, it falls under quantitative analysis and is addressed using a step function. The default value for the threshold is currently set at 0 GHz.

Following this, various optimization methods are applied. Among these, "Differential Evolution," "Bayesian," and "Bassinhopping" have proven the most efficient compared to other methods thus far. The optimization process aims to determine optimal values for E_J, E_C, E_L, and Φ_{ext} to enhance the coherence of superconducting circuits. There is also an application in optimization that includes a "sequence" option to explore repeated optimization methods multiple times and compare them with competing methods or different approaches. Moreover, exploring whether these methods converge to the same values for the qubit parameters is feasible by developing an application in Scoptimization called "Explorer". Mixing these methods and repeating iterations allows convergence to

consistent values to be observed. The software provides both numerical solutions and colorful graphical representations for predictive insights.

5.1 Scqubits - Python package

Scqubits is a Python package designed for simulating and analyzing superconducting circuits, offering convenient routines for computing energy spectra of common qubits like the Transmon, Fluxonium, Flux Qubit, etc... It facilitates visualization of spectral data, including energy level plots and matrix elements of operators, along with tools for plotting qubit wavefunctions. The package includes methods for estimating qubit coherence times (T_1, T_φ, and T_2) due to various noise channels are applied and namely T_2, called "t2_effective" is used in Scoptimization project. It also leverages multiprocessing for efficient computation and interfaces with the QuTiP package to simulate time evolution. Scqubits is utilized to construct circuits for analysis, determining factors such as coherence time and the circuit's Hamiltonian. It is a valuable tool for visualizing various variables that impact the qubit, which are utilized and evaluated by the Scoptimization Python package. More information about the functions and theory of Scqubits can be found in [30].

Chapter 6

Experimentation

At the onset of my involvement in this project, validation was the primary focus during the refinement stage of the Scoptimization Python package. The Scoptimization Python package underwent rigorous testing across diverse established qubits. Initial trials focused on the Transmon qubit (more details in Section 6.1 and 6.3.7), where the objective was to furnish minimal additional information, such as specific ratio specifications crucial for Transmon. This approach aimed to equip Scoptimization with a superconducting circuit resembling Transmon regarding components and layout. The tailored cost function for the optimization process was designed to deduce values validated by numerous scientists through experimentation. The expectation was for Scoptimization to converge towards known Transmon values. Subsequently, Fluxonium emerged as the next qubit for analysis and optimization (more details in Sections 6.2 and 6.3.5). The testing phase also involved exploring 3-node circuits (more details in Section 6.3), combining various circuit elements to unveil potential new qubit architectures.

6.1 Transmon testing

The initial phase of testing involved evaluating the Transmon qubit within this project. The objective was to replicate or surpass the results achieved by the original team. I aimed to achieve this by providing only the circuit elements and layout without specifying additional details such as ratio $E_J/E_C >> 1$. The designed cost function was expected to yield results similar to those obtained through experimental testing, if not superior. The primary parameters optimized during the process are highlighted in red in Transmon's Hamiltonian below:

$$\hat{H} = 4E_C\hat{n}^2 - E_J\cos(\hat{\varphi}).$$

6.1.1 Initialization

The initial step involves properly configuring the circuit elements for the Transmon qubit, as depicted in Figure 4.2. Transmon's energy parameters (E_J, E_C) are initialized by string type inputs using a branch system:

```
input_string = """branches:
- ["JJ",~1,2,~EJ = {},~EC = {}]
""".format(EJ,~EC).
```

The branch only mentions the Josephson junction, although the circuit has an additional capacitor element. It is not explicitly stated in the branch because the capacitance is already accounted for in calculating the charging energy, E_C. The branch is passed into the analysis phase of Scoptimization, where it is connected with Scqubits.

6.1.2 Analysis

Here, Scqubits processes the provided branch and its Hamiltonian, identifying critical influences on the circuit such as coherence time (T_2) or other noise channels. Next, analyzes anharmonicity (α - minimal, relative, and total), and Scoptimization is analyzed unbounded energy (B). It is possible to define a range, referred to as bounds, for the optimized parameters, limiting the search to values within that range. My setup for these parameters was as follows:

$$E_C = (0.01,\ 3),\ E_J = (0.1,\ 10).$$

I had two available options. Firstly, I could let the optimization process generate its starting values and then optimize them, which is done later in Section 6.1.5. Alternatively, I could manually input parameter values into a dictionary, specifying the number of points for each parameter. I selected the second choice, using a parameter dictionary approach, as it provided me with a level of control to monitor, guide the process, and easily detect errors in values resulting from the construction of the cost function. I use a total of 40 points, resulting in 1600 different combinations. The setup bounds constrained these points and later fed into the sweep function, illustrating combinations of E_J and E_C values alongside their contribution values as shown in Figure 6.1. These contributions were added to produce the final value of the cost function.

	EJ	EC	t2_effective	qualitative_anharmonicity	quantitative_anharmonicity	quantitative_unbound	cost_function
0	0.1	0.010000	1.262634e-06	-0.025499	4.0	0.0	3.974503
1	0.1	0.086667	6.565970e-07	-0.344275	0.0	4.0	3.655726
2	0.1	0.163333	3.695722e-07	-0.652060	0.0	4.0	3.347941
3	0.1	0.240000	2.569130e-07	-0.959133	0.0	4.0	3.040868
4	0.1	0.316667	1.978361e-07	-1.266009	0.0	4.0	2.733991
...	...	...	...	...	...	...	...
1595	10.0	2.693333	5.293840e-05	-10.038147	0.0	4.0	-6.038094
1596	10.0	2.770000	5.347648e-05	-10.363178	0.0	4.0	-6.363124
1597	10.0	2.846667	5.398389e-05	-10.687368	0.0	4.0	-6.687314
1598	10.0	2.923333	5.446192e-05	-11.010770	0.0	4.0	-7.010715
1599	10.0	3.000000	5.491181e-05	-11.333431	0.0	4.0	-7.333376

Figure 6.1: Table displaying the combinations of parameter dictionary values set for E_J and E_C (total points = 1600), which I defined. It presents the resulting values for anharmonicity α, coherence time T_2, and unboundedness B, culminating in the final cost function value derived from these contributions.

6.1.3 Single optimization

My landscape setup is ready for optimization. I used the most effective optimization method for the single-run optimization: Differential Evolution. The optimization uses the landscape data points as a starting point, generating an additional 67 points to determine the optimal values. The optimization method used the set bounds and the 'best2exp' strategy, setting the maximal iterations to 1000 and population size to 20 and enabling the 'polish' feature. Two other optimization methods (Bassinhopping and Bayesian) were considered for this process, but they yielded similar results compared to each other.

I was provided graphical and numerical results from a simulator designed explicitly for Transmon characteristics. My primary goal was to replicate these results using Scoptimization, which does not include Transmon-specific features. Despite this, I achieved very satisfactory results, as demonstrated in Figure 6.2.

In Figure 6.2(a), the results from the optimization show combinations of different E_J and E_C values used to compute T_2 effective. The "optimal" value is marked by a red star, indicating the highest T_2 value for this instance. Figure 6.2(b) illustrates the qualitative anharmonicity, highlighting the highest anharmonicity in the high ratio region. Figure 6.2(c) presents the penalty region for anharmonicity, emphasizing the need to push it above a certain threshold to avoid unrealistic ratios and nonsensical energy parameter values. Figure 6.2(d) displays the unbound penalty, indicating whether the excited state is outside the bounds, which would create an unusable qubit. The final graphical figure, Figure 6.2(e), is the cost function, viewed as a combination of the previous Figures (6.2(a)-(d)). The corresponding optimal values, ratios, and resulting contribution values are shown numerically in Figure 6.2(f). The ratio presented is decent, though slightly lower than expected, yet still sufficient to classify this as a Transmon qubit based on the results. The coherence time is somewhat shorter than anticipated, and the anharmonicity is high but does not exceed unrealistic boundaries. The unboundedness converges to 0, and this result is correct.

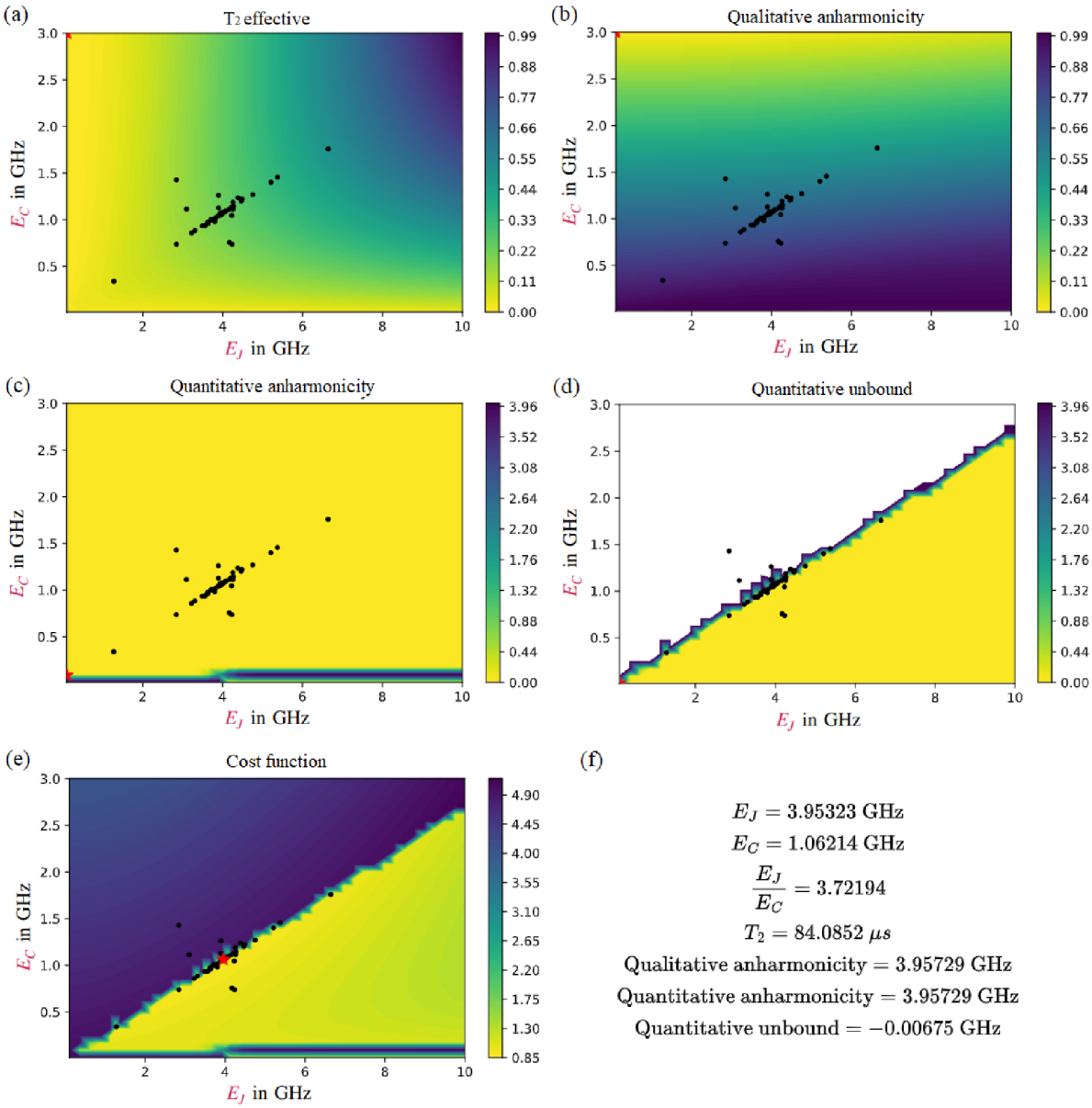

Figure 6.2: Single optimization of Transmon. (a) Optimization results show combinations of different E_J and E_C values used to compute T_2 effective. The "optimal" value is marked by a red star, indicating the highest T_2 value for this instance. (b) Qualitative anharmonicity, highlighting the highest anharmonicity in the high ratio region. (c) Penalty region for anharmonicity, emphasizing the need to push it above a certain threshold to avoid unrealistic ratios and nonsensical energy parameter values. (d) An unbound penalty indicates whether the excited state is outside the bounds, which would create an unusable qubit. (e) The cost function combines the previous figures (a)-(d). (f) Corresponding optimal values, ratios, and resulting contribution values.

6.1.4 Sequence optimization

a "Sequence" is a type of application in Scoptimization that combines different optimization methods. Currently, only three optimization methods are applicable: Differential Evolution, Bayesian, and Basinhopping. My approach initially involved applying all three. This sequential process assessed whether these methods converged to the same solution or provided different outcomes, aiming for increased efficiency and precision. It uses the same dataset as in Section 6.1.3. After the initial optimization, I expanded the dataset with 85 additional data points through sequence application, displayed in 6.3. The results in Figures 6.2(a)-(f) are very similar, showing consistency across different optimization methods. While these methods have explored additional points for potentially better solutions, they converge to negligibly different values. These values are numerically equivalent, as shown in Figure 6.2(f).

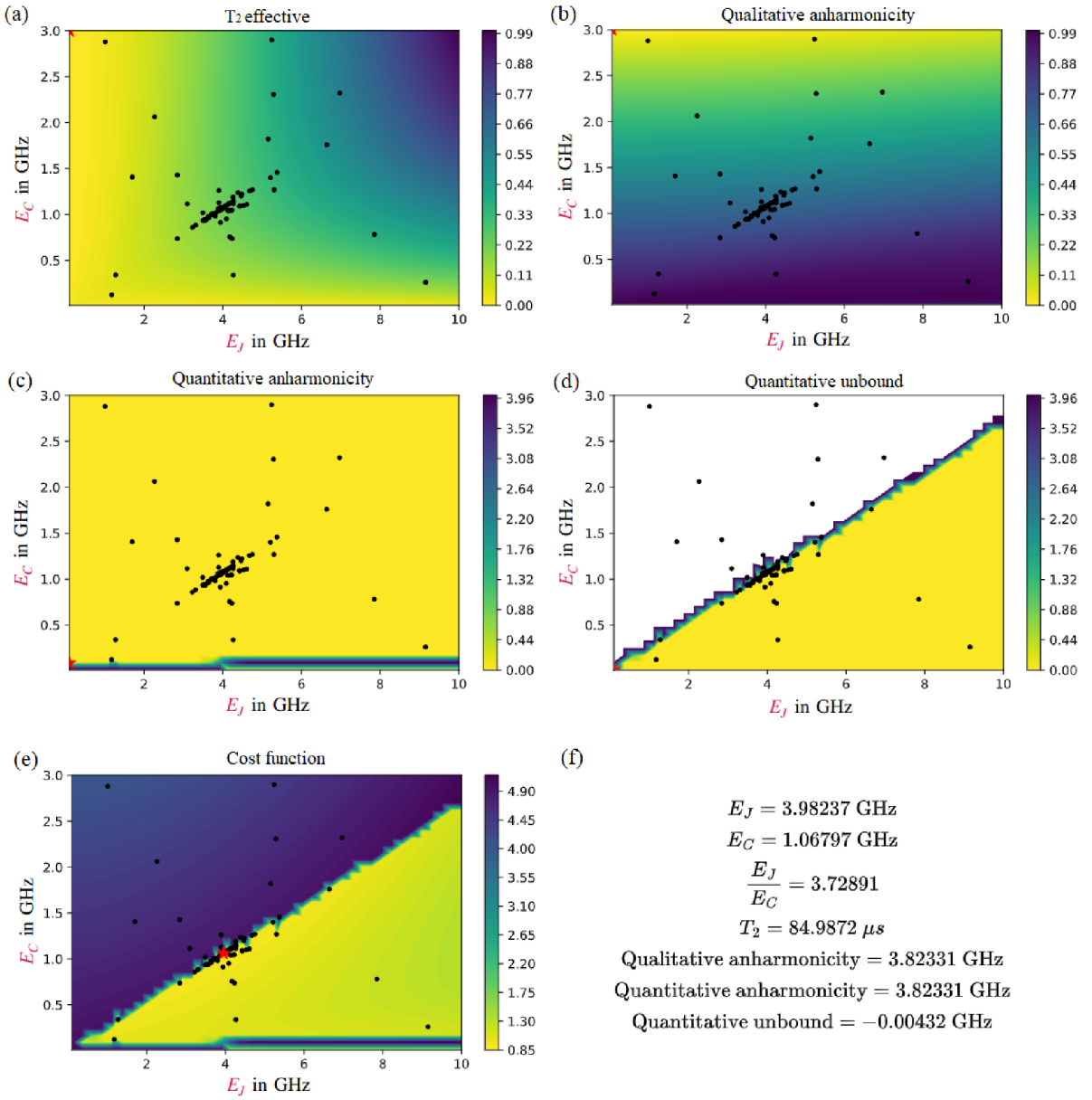

Figure 6.3: Sequence optimization of Transmon. (a) The optimization results illustrate combinations of different E_J and E_C values used in computing the effective T_2. The "optimal" value, denoted by a red star, represents the highest T_2 value attained for this particular instance. (b) Qualitative anharmonicity is depicted, emphasizing the highest anharmonicity within the high ratio region. (c) The penalty region for anharmonicity underscores the importance of surpassing a certain threshold to prevent unrealistic ratios and nonsensical energy parameter values. (d) An unbound penalty evaluates whether the excited state falls outside the predefined bounds, which would render the qubit unusable. (e) The cost function presents a composite view derived from the preceding figures (a)-(d). (f) Corresponding optimal values, ratios, and resulting contribution values are displayed numerically.

6.1.5 Explorer optimization

The "Explorer" is another application within the Scoptimization package. It streamlines the optimization process by allowing it to determine its initial points and find optimal values without requiring a parameter dictionary like before. My approach involved configuring an optimization method to repeat itself three times within a single run. Subsequently, these runs were repeated three times. The purpose of executing the same approach three times was to assess whether the optimization method arrived at consistent conclusions, which are graphical and numerical results shown in Figure 6.4.

Figure 6.4(a) illustrates a lower-than-expected ratio and a very short coherence time, contrary to the anticipated duration of at least hundreds of microseconds. It is crucial to note that in this scenario, the anharmonicity is too high to be experimentally feasible. The second run shown in Figure 6.4(b) displays a similar ratio but offers different optimized values for E_J and E_C, leading to a higher coherence time, although still insufficient. The anharmonicity remains too high for the qubit's driving frequency, posing experimental challenges. The final optimization run in Figure 6.4(c) exhibits a similar ratio and very low coherence time due to increased anharmonicity, aligning with previous discussions on the inverse relationship between anharmonicity and coherence time. Despite these limitations, these results suggest the correct direction and validate the expected behavior of Transmon, which will be further explored in Section 6.3.7.

(a)

$$E_J = 5.88767 \text{ GHz}$$
$$E_C = 1.58290 \text{ GHz}$$
$$\frac{E_J}{E_C} = 3.71951$$
$$T_2 = 44.9934\ \mu s$$
Qualitative anharmonicity = 5.89805 GHz
Quantitative anharmonicity = 5.89805 GHz
Quantitative unbound = −0.00568 GHz

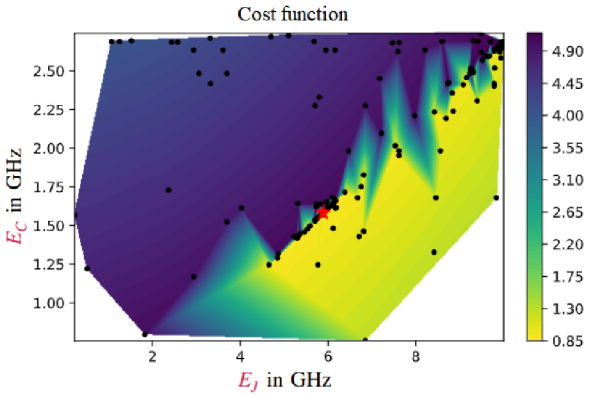

(b)

$$E_J = 4.79255 \text{ GHz}$$
$$E_C = 1.28812 \text{ GHz}$$
$$\frac{E_J}{E_C} = 3.72057$$
$$T_2 = 62.4032\ \mu s$$
Qualitative anharmonicity = 4.79949 GHz
Quantitative anharmonicity = 4.79949 GHz
Quantitative unbound = −0.00614 GHz

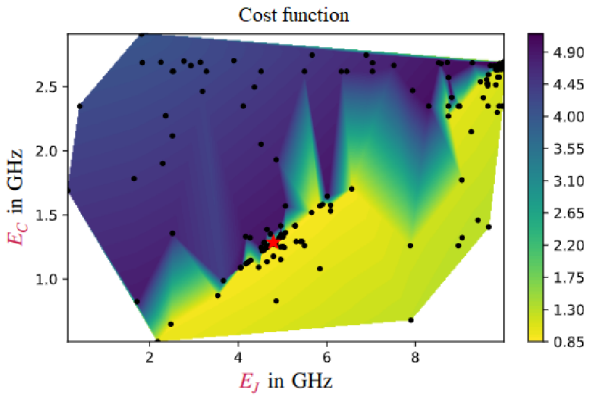

(c)

$$E_J = 8.31351 \text{ GHz}$$
$$E_C = 2.23565 \text{ GHz}$$
$$\frac{E_J}{E_C} = 3.71861$$
$$T_2 = 25.6534\ \mu s$$
Qualitative anharmonicity = 8.33055 GHz
Quantitative anharmonicity = 8.33055 GHz
Quantitative unbound = −0.00563 GHz

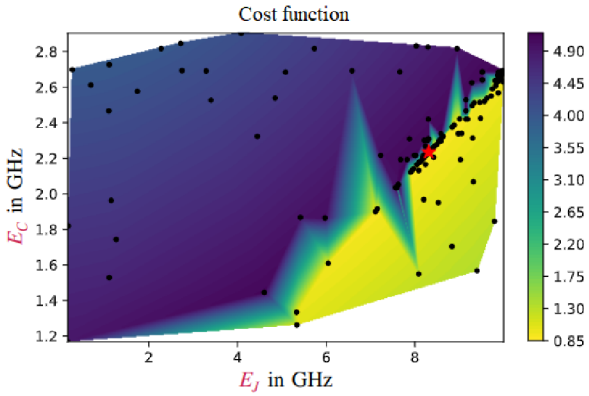

Figure 6.4: Transmon optimization using Scoptimization "Explorer" type application. (a) Illustrates a lower-than-expected ratio and a very short coherence time T_2, contrary to the anticipated duration of at least hundreds of microseconds. It is crucial to note that in this scenario, the anharmonicity α is too high to be experimentally feasible. (b) It displays a similar ratio but offers different optimized values for E_J and E_C, leading to a higher coherence time T_2, although it is still insufficient. The anharmonicity α remains too high for the qubit's driving frequency, posing experimental challenges. (c) It exhibits a similar ratio and very low coherence time due to increased anharmonicity, aligning with previous discussions on the inverse relationship between anharmonicity and coherence time. Despite these limitations, these results suggest the correct direction and validate the expected behavior of Transmon.

6.2 Fluxonium Testing

Testing a single qubit to validate the accuracy of a new application is not efficient enough. Therefore, I aim to explore Fluxonium, which incorporates an additional circuit element - inductor L - parallel-connected to the Transmon circuit. This arrangement generates an external flux (Φ_{ext}) that facilitates further qubit manipulation while introducing new noise sources (flux noise). As a result, this leads to a new Hamiltonian and additional parameters for optimization. Four parameters, denoted in red, are particularly emphasized in the Fluxonium's Hamiltonian:

$$\hat{H} = 4E_C\hat{n}^2 - E_J\cos(\hat{\varphi} - \Phi_{ext}) + \frac{1}{2}E_L\hat{\varphi}^2.$$

The process for Fluxonium testing followed the same steps as for Transmon. The first step is to initialize the circuit, which is shown in the form of the branches below:

```
input_string = """branches:
- ["JJ",~1,2,~EJ = {},~EC ={}]
- ["L",~1,2,~EL = {}]
""".format(EJ,~EC,~EL)
```

Initially, these parameters are assigned placeholder values. However, parameters set to bounds will be optimized during the optimization process, while parameters with placeholder values will remain static, initializing the circuit, particularly its Hamiltonian.

I could access pre-simulated graphical and numerical results from a simulator designed explicitly for Fluxonium. With numerous variables to optimize, the challenge lies in determining crucial parameters and prioritizing their optimization. I focused on optimizing only two parameters: E_J and Φ_{ext}, providing insight into Fluxonium's behavior and validating the software's functionality. This approach helps identify optimal operating conditions, such as the sweet spot for external flux, maximizing qubit performance.

6.2.1 Analysis

I configured the optimization landscape using a parameter dictionary with 150 points per optimized parameter. Additionally, I included sweet spots for the external flux values as follows:

$$\text{sweet spots} = [0.0, 0.33, 0.5, 0.88, 1.0],$$

where $\Phi_{ext} = 0.5$ is the critical value declared as the optimal sweet spot for coherence time. These values were necessary to ensure that the optimization process did not overlook them. With two swept parameters, this results in 22,950 points, as illustrated in Figure 6.5. I also defined bounds for E_J and Φ_{ext}, while I set initial and steady values for E_C and E_L. The bounds and values are as follows:

$$E_J = (0.01,\ 8.0),\ \Phi_{ext} = (-0.1,\ 1.1),\ E_C = 1.5,\quad E_L = 0.5.$$

	EJ	Φ1	t2_effective	qualitative_anharmonicity	quantitative_anharmonicity	cost_function
0	0.01	-0.100000	7.380084e-06	-0.051680	4.0	3.948327
1	0.01	-0.091946	7.384985e-06	-0.051817	4.0	3.948191
2	0.01	-0.083893	7.384189e-06	-0.051943	4.0	3.948064
3	0.01	-0.075839	7.377700e-06	-0.052059	4.0	3.947949
4	0.01	-0.067785	7.365537e-06	-0.052163	4.0	3.947844
...	...	...	...	...	...	...
22945	8.00	1.091946	5.938996e-04	-1.550631	0.0	-1.550037
22946	8.00	1.100000	4.823630e-04	-2.097365	0.0	-2.096883
22947	8.00	0.000000	1.712811e-05	-2.237983	0.0	-2.237966
22948	8.00	0.500000	5.662654e-07	-0.706663	0.0	-0.706662
22949	8.00	1.000000	1.712811e-05	-2.237983	0.0	-2.237966

Figure 6.5: Table displaying the combinations of parameter dictionary values set for E_J and Φ_{ext} (total points = 22950), which I defined. It presents the resulting values for anharmonicity α, coherence time T_2, and unboundedness B, culminating in the final cost function value derived from these contributions in the last column.

6.2.2 Single optimization

I configured the landscape to assess whether the cost function could identify the optimal points for this qubit. Due to the complexity of the search space, the optimization process was extensive, involving 22,950 points. For Fluxonium optimization, I employed the differential evolution method, setting predefined boundaries and allowing a maximum of 300 iterations. The 'rand2exp' strategy was chosen for its superior effectiveness, utilizing a population size of 20.

Ultimately, the optimization yielded an additional 120 points, and the resulting optimal values are displayed in Figure 6.6. Figure 6.6 displays the optimal values for the Josephson energy E_J and external flux Φ_{ext}. These values align with expectations, reaching the sweet spot of 0.5, as anticipated. Subsequently, qualitative and quantitative assessments of anharmonicity are depicted in (b) and (c), respectively. Notably, it is a binary indicator dependent on the values derived in (b). The final cost function, illustrated in (d), showcases a deviation from the anticipated value. However, tighter bounds on E_J (ranging from 0.01 to 5.0) could have yielded closer alignment with the expected sweet spot. These figures offer a comprehensive view of the contributions involved in the overall cost function. Additionally, it is important to note that due to the presence of the inductor, the calculation of boundedness is omitted, as the quadratic term introduces a quadratic well. Figure 6.7 shows the corresponding numerical results below.

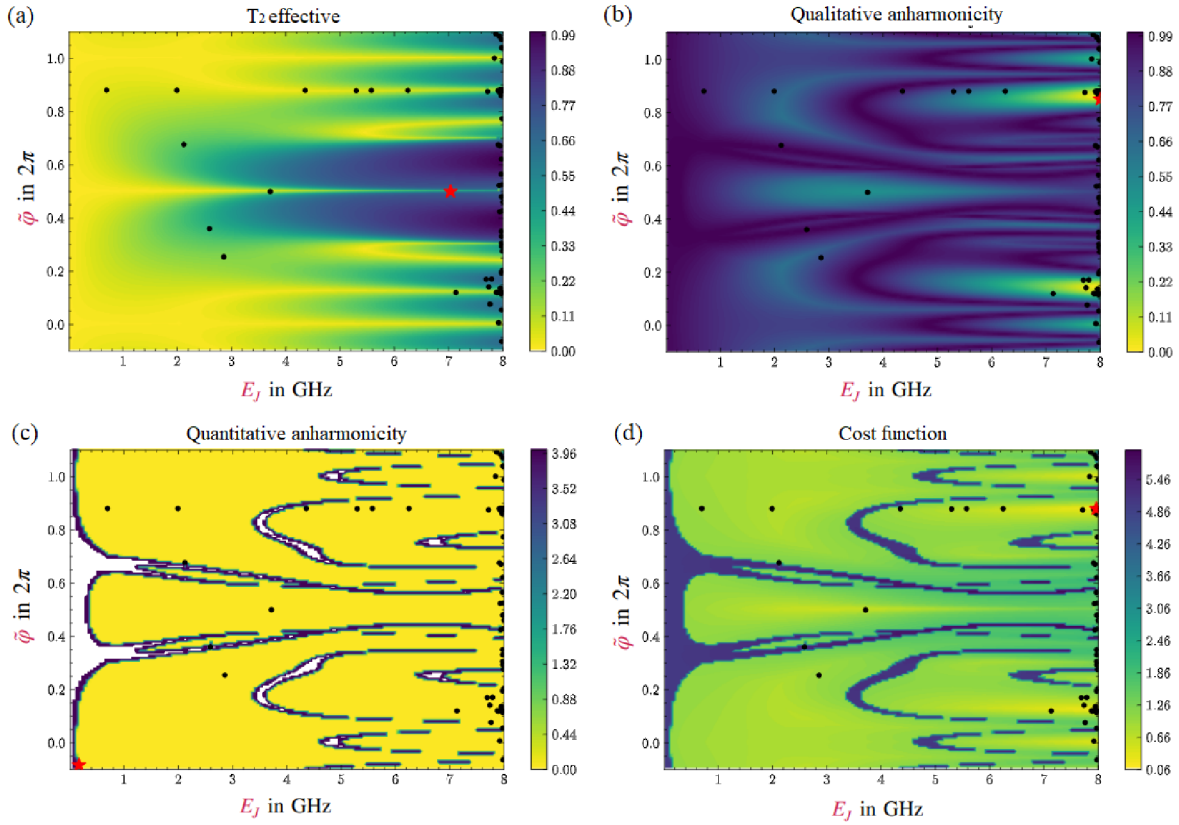

Figure 6.6: Fluxonium single optimization run test. (a) The optimization results showcase various combinations of E_J and Φ_{ext} values utilized in computing the effective T_2. A red star marks the "optimal" value, representing the highest attained T_2 for this instance, derived at the sweet spot $\Phi_{ext} = 0.5$. Qualitative anharmonicity (b) emphasizes the highest anharmonicity, which is found at $\Phi_{ext} = 0.33$ or 0.88. The penalty region for anharmonicity (c) highlights the necessity of surpassing a certain threshold to avoid unrealistic ratios and nonsensical energy parameter values. The sum of the contributions (a)-(c) results in the (d) final cost function, where its numerical results are displayed in Figure 6.7.

$$E_J = 7.96533 \text{ GHz}$$
$$\Phi_{\text{ext}} = 0.88004$$
$$T_2 = 37.0058\ \mu s$$
$$\text{Qualitative anharmonicity} = 3.06834 \text{ GHz}$$
$$\text{Quantitative anharmonicity} = 3.06834 \text{ GHz}$$

Figure 6.7: Fluxonium single optimization run. The numerical results that were produced and graphically displayed in Figure 6.6(d).

6.3 3 node general circuit optimization

This chapter involves advancing testing methodologies beyond software debugging to encompass the identification and resolution of issues across various testing levels. The testing framework was crafted utilizing a 3-node circuit system, as depicted in Figure 6.8(a). It comprises three nodes with empty circles, capable of accommodating elements showcased in Figures 6.8(b)-(e).

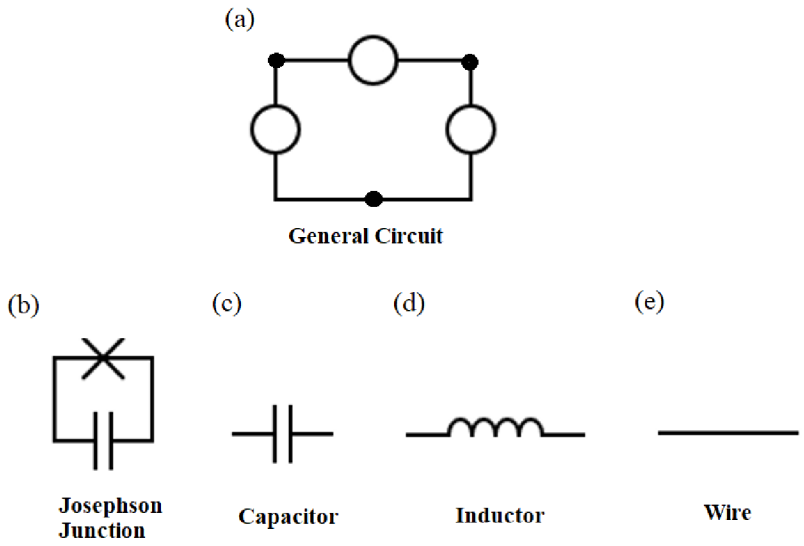

Figure 6.8: 3-node circuit and elements. (a) It depicts a circuit with three empty circular nodes to be filled by different circuit elements, as shown in (b)-(e). (b) It represents the Transmon circuit design, symbolized by a Josephson junction in subsequent analyses. (c) a capacitor. (d) An inductor. (e) a wire is used to close the loop.

The primary component, depicted in Figure 6.8(b), represents the Transmon circuit type, denoted solely by the Josephson junction symbol. From this point onward, the discussion of Josephson junctions will primarily focus on those connected in parallel with a capacitor, resulting in Transmon. Additionally, Figures 6.8(c) and (d) showcase familiar circuit components— a capacitor and an inductor—while Figure 6.8(e) introduces a "filler" or superconducting wire crucial for loop closure.

The number of unique combinations that can be formed from 4 elements occupying 3 empty spaces is calculated as $4! = 24$. Figure 6.9 illustrates these permutations, with red rectangles highlighting potential superconducting circuits. Other configurations are deemed unsuitable due to the absence of Josephson junctions or their inability to form viable circuits.

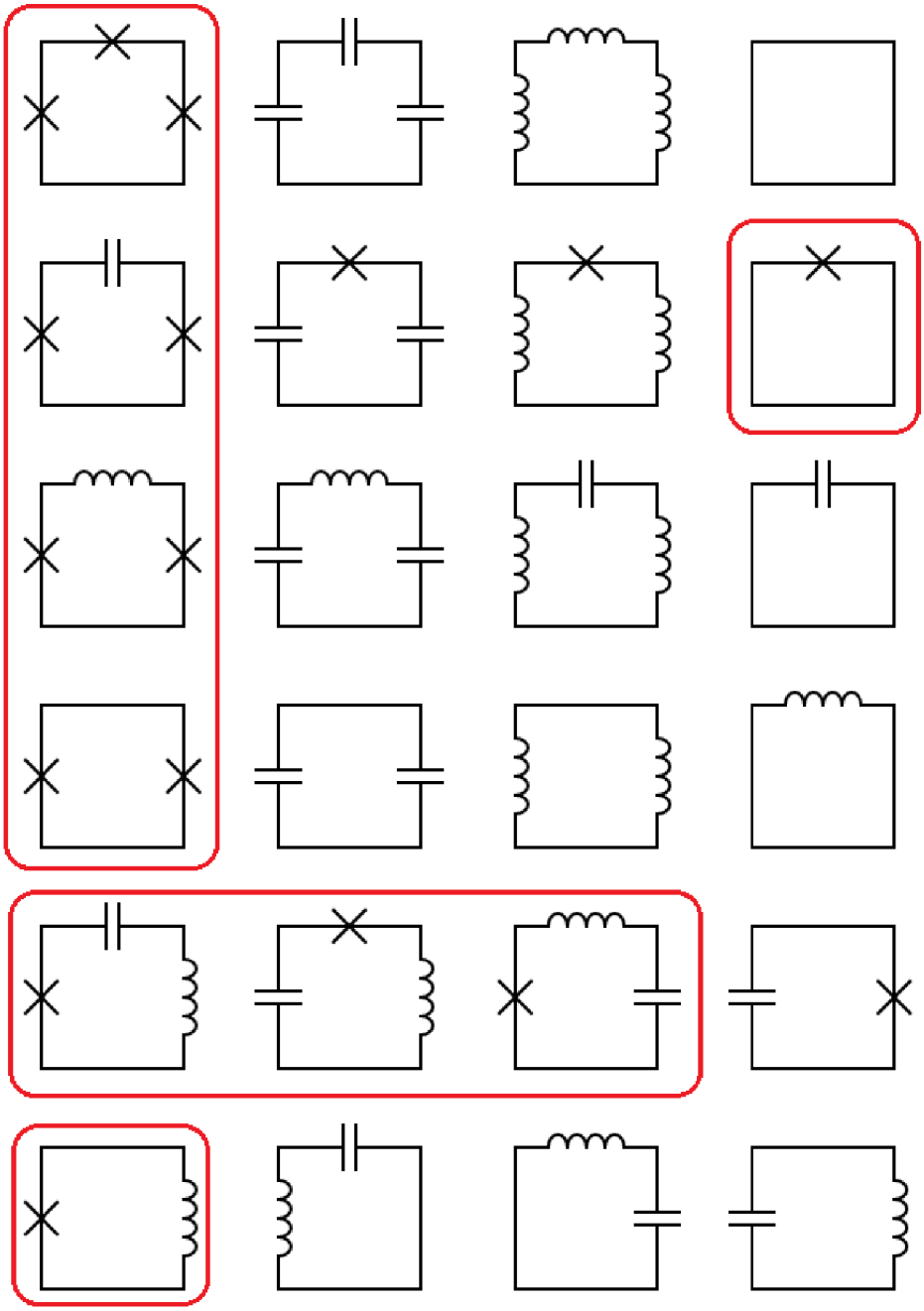

Figure 6.9: 24 possible combinations of 3-node circuits using 4 elements. The circuits highlighted in red rectangles indicate potentially viable qubits that will be further tested and optimized.

The circuits with the potential to uncover novel insights and optimizations are showcased alongside their corresponding testing labels in Figure 6.10. Various optimizations will be applied to the circuits to determine the most favorable outcomes. Additionally, a key consideration revolves around balancing theoretical feasibility with practical experimental application, which I will address for each circuit. Within this ensemble of circuits, I encounter established designs that have already been identified and studied, including the Flux Qubit depicted in Figure 6.10(a), SQUID in Figure 6.10(d), Fluxonium in Figure 6.10(e), and Transmon in Figure 6.10(f).

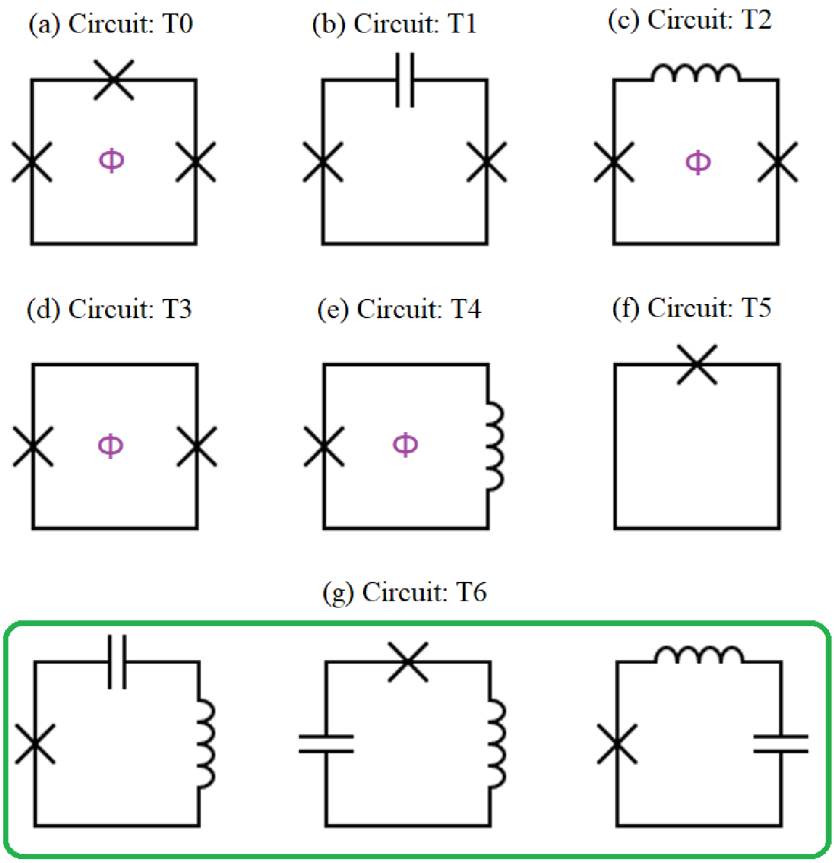

Figure 6.10: 7 potential circuit combinations, using symbolic representation for the Josephson junctions to denote Transmon circuit designs. "Josephson junction" refers to the Transmon circuit in these circuits. (a) T0 circuit consists of 3 Josephson junctions and an external magnetic flux Φ (purple). This configuration is known as Flux Qubit. (b) T1 circuit includes 2 Josephson junctions and a capacitor. (c) T2 circuit comprises 2 Josephson junctions and a linear inductor, forming a closed loop with external magnetic flux. (d) T3 circuit contains 2 Josephson junctions and generates an external magnetic flux known as SQUID. (e) T4 circuit features 1 Josephson junction and a linear inductor, creating a closed loop with external magnetic flux, recognized as Fluxonium. (f) T5 circuit incorporates 1 Josephson junction, representing the Transmon circuit. (g) T6 circuit includes 1 Josephson junction, a capacitor, and an inductor.

I encounter various conditions affecting optimal outcomes, such as identifying unchanged static parameters during optimization runs and defining suitable bounds for them. Initially guided by intuition, these bounds aim to minimize interference with optimization processes while troubleshooting circuit failures. Adjusting bounds allows the

exploration of different parameter regions, preventing unintended convergence. I prefer an exploratory approach over predefined parameter dictionaries, as seen in Sections 6.1.3 and 6.2.2. Experimenting with point variations during optimization helps gauge their impact. Primarily, the optimization will produce results for coherence time (T_2), anharmonicity (α), and, if applicable, unboundedness (B). I will identify sweet spots, especially with external flux, and examine optimal Hamiltonian values to discern new qubit creation or convergence to known qubits or harmonic oscillators.

The first test will showcase the results for the longest coherence time, while the second test will highlight a feasible circuit that could theoretically be considered for engineering. The graphical results will use color coding: T_2 is denoted in blue, α in yellow, B in green, and Φ_{ext} in brown. Corresponding numerical values for each circuit will be displayed in table form below.

6.3.1 T0 circuit - results and discussion

The first circuit comprises 3 Josephson junctions, forming a closed loop and generating external magnetic flux. This established qubit, as the Flux Qubit, is depicted in Figure 6.11.

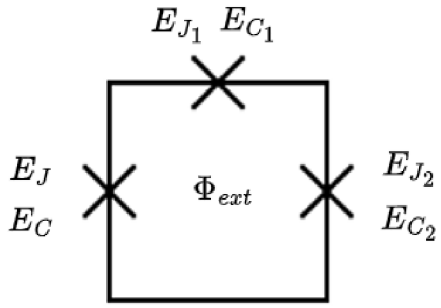

Figure 6.11: T0 circuit contains 7 parameters: E_J, E_C, E_{J_1}, E_{C_1}, E_{J_2}, E_{C_2}, and Φ_{ext}. There can be only found 3 Josephson junctions.

For a successful Flux Qubit, the key characteristics are tuning the external magnetic flux to the sweet spot $\Phi_{\text{ext}} = 0.5$ and achieving identical ratios for the first and second Josephson junctions ($E_J/E_C = E_{J_2}/E_{C_2}$). The third Josephson junction should have its Josephson energy and charging energy adjusted such that $E_{J_1} = E_J\beta$ and $E_{C_1} = E_C/\beta$, where β ranges between 0.4 and 0.7, altering the shape of the potential well [31].

The circuit encompasses seven parameters: E_J, E_C, E_{J_1}, E_{C_1}, E_{J_2}, E_{C_2}, and Φ_{ext}. My optimization efforts involved numerous iterations, experimenting with different bounds, and adjusting the cost function. I present two notable results: "TEST E," which represents optimization yielding the longest coherence time, and "TEST F," engineered to fit specific characteristics. Figure 6.14 shows the numerical values for optimized parameters and contributions.

Two tests are illustrated in Figure 6.12. In "TEST E," I set fixed values for one Josephson junction ($E_J = 35$ GHz and $E_C = 1$ GHz) while leaving the bounds open for the other two. Strict boundaries were imposed on the magnetic flux to achieve the sweet spot value $\Phi_{\text{ext}} = 0.5$. Despite yielding the longest coherence time T_2, this qubit

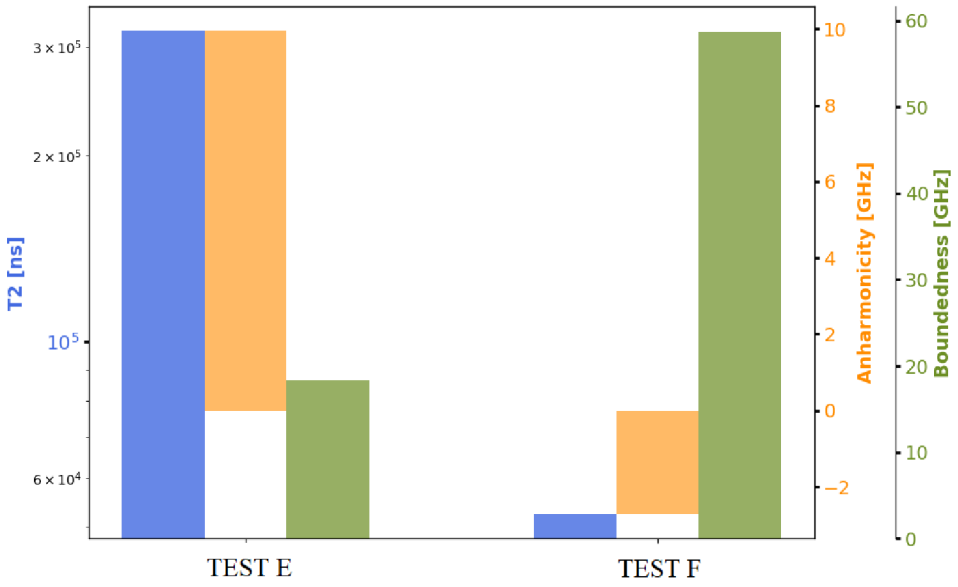

Figure 6.12: T0 circuit results: (coherence time (T_2), anharmonicity (α), and boundedness (B)). The optimization for 'TEST E' yielded the longest coherence time, indicating promising performance for this qubit. 'TEST F' demonstrates characteristics potentially suitable for a flux qubit. Numerical values are shown in Figure 6.14.

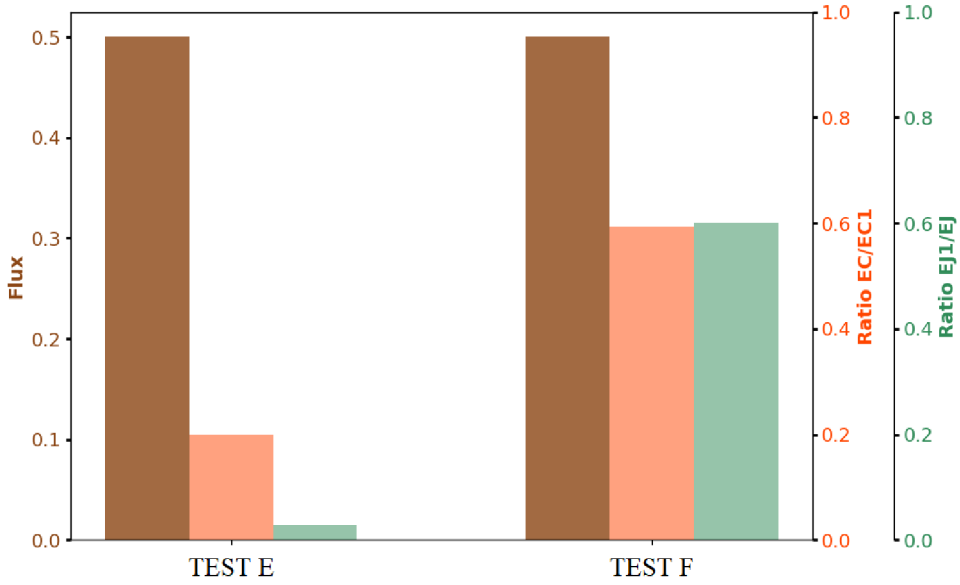

Figure 6.13: T0 circuit results of flux (Φ_{ext}), ratio ($E_J/E_C = \beta$), and ratio ($E_{J_1}/E_{C_1} = \beta$) for "TEST E" and "TEST F". Numerical values are shown in Figure 6.14.

configuration is deemed unfeasible due to its high anharmonicity, while boundedness is pretty low compared to the other tests.

In Figure 6.13, "TEST E" results reveal the impact of imposing strict bounds on external magnetic flux, resulting in distinct sweet spot outcomes. Furthermore, inconsistencies in the β ratio between Josephson and charging energies are observed, with significant deviations. The derived optimal values exhibit characteristics more akin to a Transmon qubit than a Flux Qubit, rendering them nonviable for the intended purpose.

In Figure 6.12, "TEST F" is displayed, showcasing Flux Qubit characteristics as depicted in Figure 6.13. It reveals the sweet spot for external magnetic flux and ensures the β value falls within the specified range. However, despite meeting the expected properties, the coherence time is notably short, as shown in Figure 6.12, compared to experimental results illustrated in Figure 2. Additionally, the negative anharmonicity indicates a switch between the ground and first excited states. Although the anharmonicity appears low, the exceptionally high boundedness suggests potential issues with the cost function defining the qubit's constraints, given its magnitude.

	EJ	EC	EJ1	EC1	EJ2	EC2	ϕ	T2	α	B	EJ1/EJ	EC/EC1
TEST E	35	1	1.0071	5	1.0001	5	0.5	318793	9.958	18.281	0.0288	0.2
TEST F	35	1	20.99	1.69	35.01	0.99	0.5	52381	-2.724	58.72	0.5997	0.5917

Figure 6.14: T0 circuit - numerical results.

6.3.2 T1 circuit - results and discussion

This circuit is constructed with 2 Josephson junctions and a capacitor, as illustrated in the provided Figure 6.15. Notably, there is no flux to contend with, simplifying the optimization process and eliminating concerns about sweet spots.

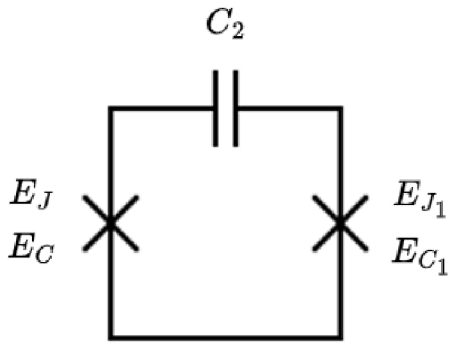

Figure 6.15: T1 circuit contains 5 parameters: E_J, E_C, E_{J_1}, E_{C_1}, and E_{C_2}.

I anticipate Josephson junctions will exhibit ratios within the flux regime (the Transmon ratio), while the additional capacitor should enhance the stability of energy levels. However, I do not expect this qubit to be the leading one, as issues with charging noise have already been identified and addressed. The tests that produced the longest coherence time and the most doable qubit are shown below and discussed in Figures 6.16 and

6.17; the corresponding numerical results and optimal values for the circuit are shown in Figure 6.18.

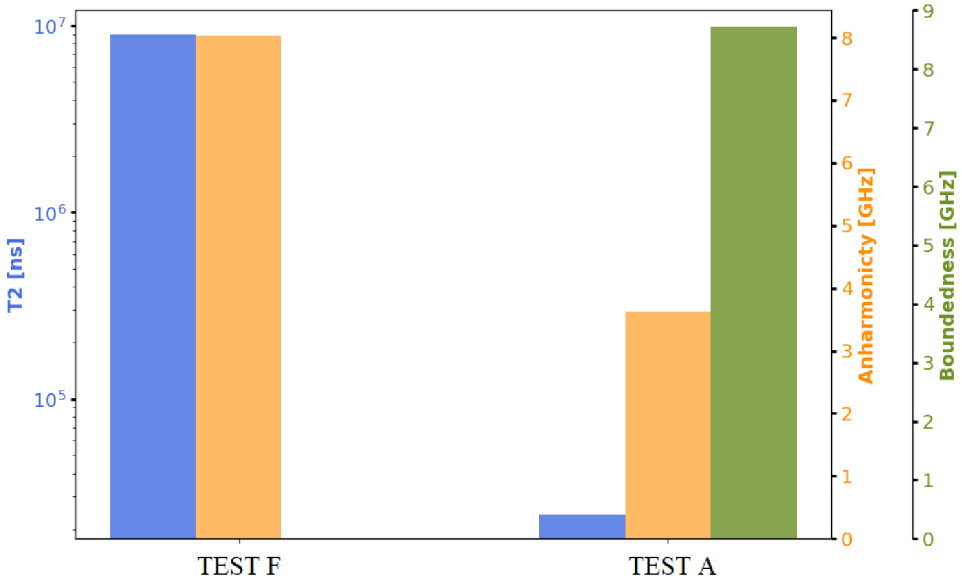

Figure 6.16: T1 circuit results - (coherence time (T_2), anharmonicity (α), and boundedness (B)). The optimization for "TEST F" yielded the longest coherence time. "TEST A" demonstrates characteristics potentially suitable for this qubit. Numerical values are shown in Figure 6.18.

In Figure 6.16, "Test F" exhibits the longest coherence time, although the anharmonicity is excessively high. However, the boundedness is relatively low, which is a promising result, albeit with an issue in anharmonicity. I configured this qubit with a fixed capacitor set to $C_2 = 6$ GHz, while leaving the rest with high bounds range, resulting in the ratios displayed in Figure 6.17, "Test F" yields results for ratios, that indicate a potential problem. One ratio approaches 0, suggesting the absence of the Josephson junction and resulting in a Transmon-like qubit, which does not introduce anything new.

On the contrary, in "Test A," as shown in Figure 6.16, I allowed all parameters to have open bounds to observe where the qubit naturally settles its values. While it generates pretty decent parameter values, it falls short regarding contributions. With a very short coherence time, it does not offer much discovery potential. While the anharmonicity is reasonable and feasible, the high boundedness indicates room for improvement. This could imply a need to refine the cost function, mainly when multiple Josephson junctions are involved in the circuit. Figure 6.17 further emphasizes similarities to "Test F," with ratios for both Josephson junctions falling within the flux regime. However, this configuration holds promise as a new qubit.

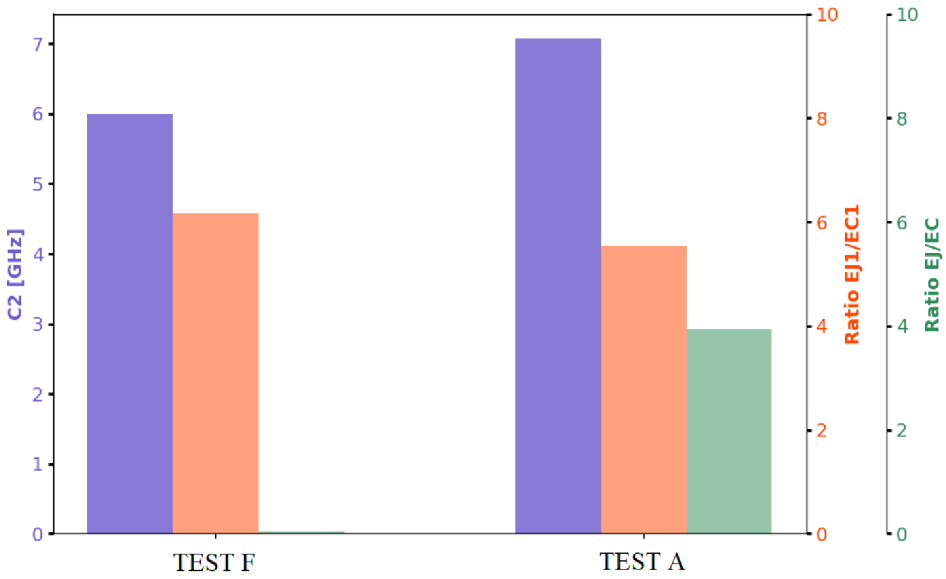

Figure 6.17: T1 circuit results of the capacitor (C_2), ratio (E_J/E_C), and ratio (E_{J_1}/E_{C_1}) for "TEST F" and "TEST A". Numerical values are shown in Figure 6.18.

	EJ	EC	EJ1	EC1	EC2	T2	α	B	EJ/EC	EJ1/EC1
TEST F	0.106	2.9987	14.95	2.4248	6	8966032.9	8.0302	0.006	0.0353	6.16537
TEST A	10.736	2.7213	7.5323	1.3606	7.0709	23998.635	3.6182	8.7174	3.9453	5.53611

Figure 6.18: Numerical optimal values and contribution results for T1 circuit.

6.3.3 T2 circuit - results and discussion

This circuit is constructed with 2 Josephson junctions and a linear inductor in a loop and creating external magnetic flux, as illustrated in the provided Figure 6.19.

I anticipate that both Josephson junctions will operate within the flux regime in this type of circuit. At the same time, the additional inductor should generate very low values due to expectations of a harmonic oscillator with high values. Furthermore, the external magnetic flux should reveal sweet spots, typically around 0.3, 0.5, or 0.88, depending on the shape it can induce, with the ideal being 0.5. I selected two tests from the optimization group testing. The first test demonstrates the longest coherence time, while the second test assesses the feasibility of the actual qubit. You can find the graphical presentation in Figures 6.20 and 6.21, and their corresponding numerical values are displayed in Figure 6.22.

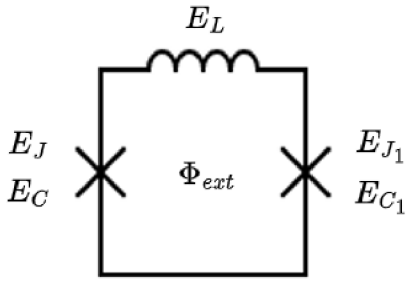

Figure 6.19: T2 circuit contains 6 parameters: E_J, E_C, E_{J_1}, E_{C_1}, E_L, and Φ_{ext}.

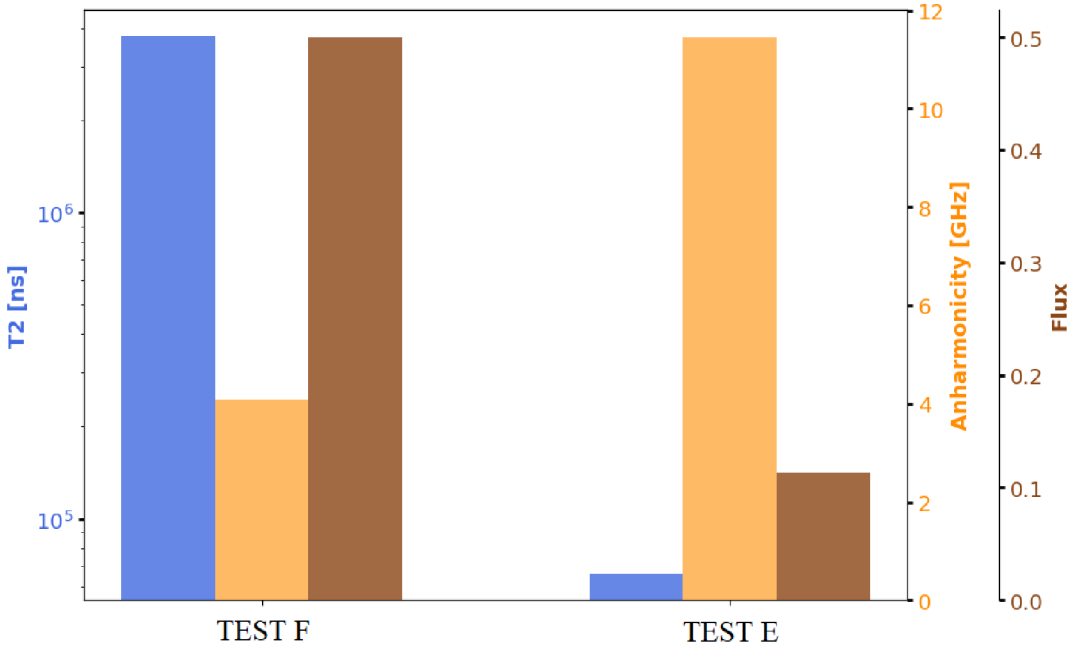

Figure 6.20: T2 circuit results - (coherence time (T_2), anharmonicity (α), and flux). The optimization for 'TEST F' yielded the longest coherence time. 'TEST E' demonstrates characteristics potentially suitable for this qubit. Numerical values are shown in Figure 6.22.

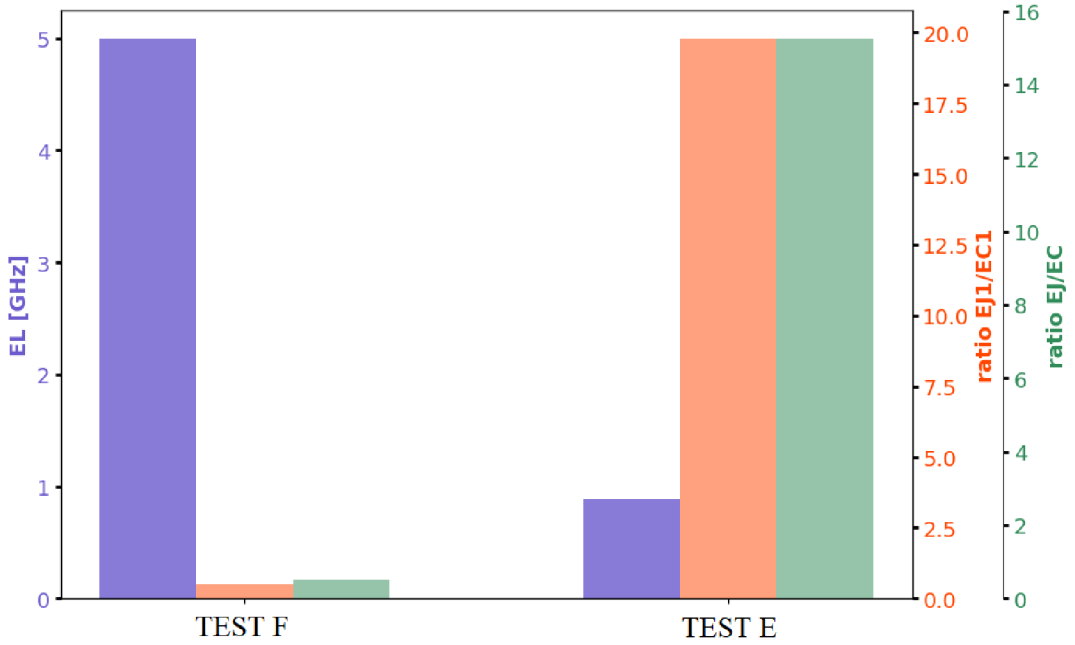

Figure 6.21: T2 circuit results of the inductor (L_2), ratio (E_J/E_C), and ratio (E_{J_1}/E_{C_1}) for "TEST F" and "TEST E". Numerical values are shown in Figure 6.22.

Figure 6.20 illustrates the "TEST F" qubit, where the charging energy for both Josephson junctions remains constant, with tight bounds applied to external flux to achieve the sweet spot of 0.5. This configuration resulted in the longest coherence time, a feasible anharmonicity, and the expected 0.5 external flux. In Figure 6.21, representing "TEST F," the high inductive energy causes this qubit to behave more like a harmonic oscillator than a potential qubit. The ratios for the Josephson junctions fall within the charging regime, confirming that this circuit behaves as a harmonic oscillator rather than a qubit.

On the other hand, "TEST E" shows more potential to be a qubit. I applied the same bounds and steady parameters, except for leaving external flux with open bounds, as shown in Figure 6.20. This resulted in a significant decrease in coherence time and a notable increase in anharmonicity. However, the anharmonicity is too high for this qubit to be feasible. I chose this test because no closer optimization for this circuit type was available, which could yield better feasibility results. The lack of guidance for external flux led to a short coherence time to be practical. However, in Figure 6.21, the ratios for the Josephson junctions fall within the flux regime, and inductive energy is relatively low, indicating less harmonic behavior. There is potential for further exploration with this circuit.

	EJ	EC	EJ1	EC1	EL	ϕ	T2	α	EJ/EC	EJ1/EC1
TEST F	1	2	1	2	5	0.5	3762673.8	4.0767	0.5	0.5
TEST E	15.255	1	19.796	1	0.8919	0.1136	66213.254	11.452	15.255	19.7959

Figure 6.22: Circuit T2: numerical results for optimization runs of "TEST F" and "TEST E".

6.3.4 T3 circuit - results and discussion

This circuit may appear similar to Flux-tunable Tranmosn qubit - SQUID, but here, it features two Transmons in the layout of a SQUID circuit, as illustrated in Figure 6.23. Since it forms a closed loop of junctions, it will exhibit external magnetic flux and have sweet spots. I anticipate producing the same result for SQUID, where more details about this qubit are explained in [**"nobreakspace −"Barrett˙2023**, 23]. the following results are displayed graphically in Figures 6.24 and 6.25, while their related numerical values are shown in Figure 6.26.

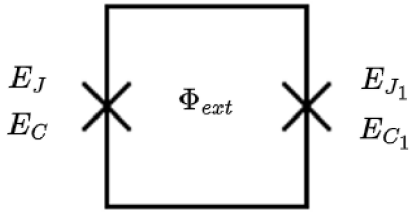

Figure 6.23: T3 circuit contains 5 parameters: E_J, E_C, E_{J_1}, E_{C_1} and Φ_{ext}.

The test labeled "TEST A" in Figure 6.24 was structured by keeping the charging energy values for both Josephson junctions static and relatively low while allowing open bounds for the rest of the parameters, including external flux. This setup resulted in a very long coherence time, good anharmonicity, and decent boundedness close to 0. However, Figure 6.25 shows that the ratios do not reach high values but instead fall between the flux and charging regimes, suggesting harmonic tendencies while still achieving sweet spot values. Although not similar to SQUID characteristics, this result produces decent parameter values. The main issue is the low ratio, leading to relatively low anharmonicity. The feasibility of this qubit remains in question, warranting further exploration.

Conversely, "TEST C" was set up with consistent values for a Josephson junction and its Josephson and charging energies. This setup resulted in a much shorter coherence time, higher anharmonicity, and significantly higher boundedness. Figure 6.25 shows ratios more fitting for a SQUID, with the external flux finding a sweet spot. This qubit has better results regarding suitability for SQUID characteristics. As previously discussed, the high boundedness may affect the low coherence time, conditioned by the cost function. The high unboundedness indicates an issue with the contribution implementation.

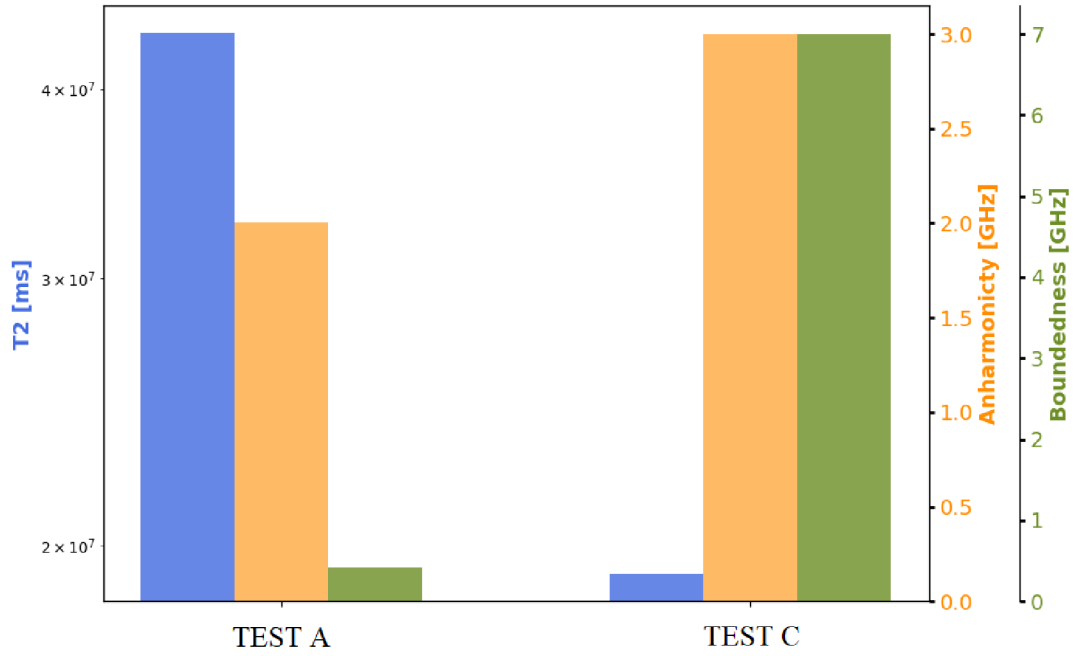

Figure 6.24: T3 circuit results - (coherence time (T_2), anharmonicity (α), and boundedness (B)). The optimization for 'TEST A' yielded the longest coherence time. 'TEST C' demonstrates characteristics potentially suitable for this qubit. Numerical values are shown in Figure 6.26.

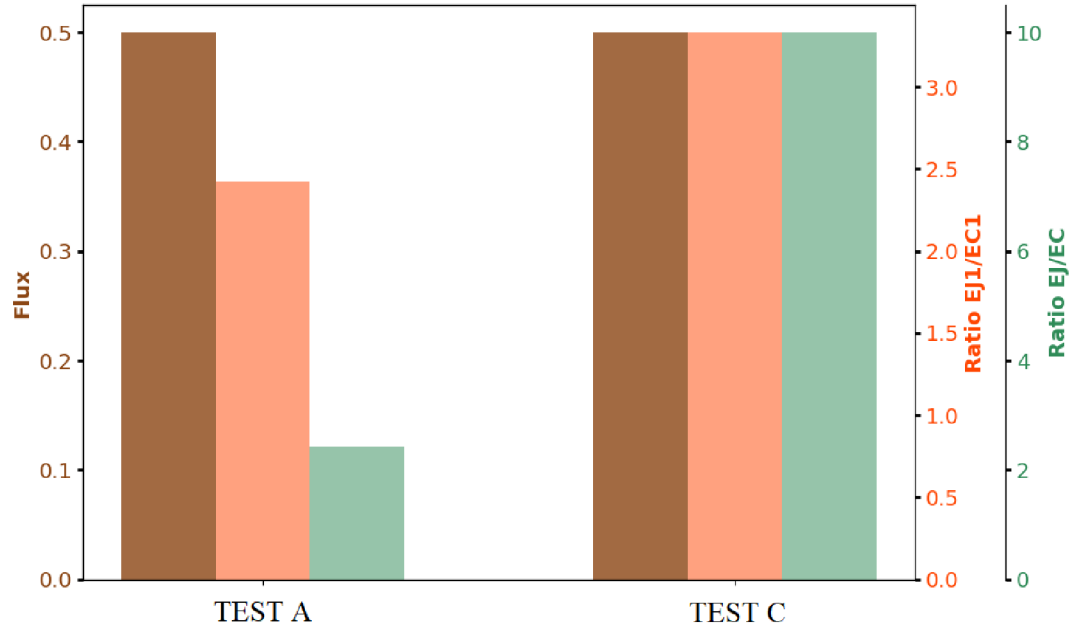

Figure 6.25: Circuit T3 results of external magnetic flux (FLUX Φ_{ext}, ratio (E_J/E_C), and ratio (E_{J_1}/E_{C_1}) for "TEST A" and "TEST C". Numerical values are shown in Figure 6.22.

	EJ	EC	EJ1	EC1	ϕ	T2	α	B	EJ/EC	EJ1/EC1
TEST A	2.42589	1	2.4253	1	0.5	43580435.8	2	0.4253	2.4259	2.4253
TEST C	10	1	9.99999	3	0.5	19158303.5	3	7	10	3.33333

Figure 6.26: Circuit T3: numerical results for optimization runs of "TEST A" and "TEST C".

6.3.5 T4 circuit - results and discussion

This circuit comprises a linear inductor and a Transmon qubit, here symbolized as Josephson junction, as depicted in Figure 6.27. Since it is parallelly connected, it forms a well-known qubit called Fluxonium. I aim to achieve long coherence and thoroughly verify its direction, as discussed in Section 4.3. I performed a single optimization run with a parameter dictionary that can be found in Section 6.2

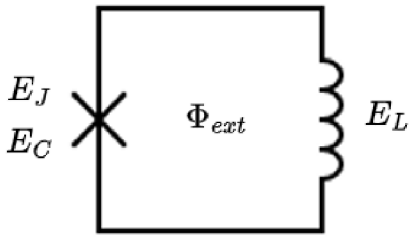

Figure 6.27: T4 circuit contains 4 parameters: E_J, E_C, E_L, and Φ_{ext}.

In the first, "TEST F," I optimized the Josephson junction parameter values while keeping the inductive energy and external flux steady. This approach achieved a high coherence time, though with negative anharmonicity, indicating that the first excited and ground states switched. The results are displayed in Figure 6.28.

In the second test, "TEST D," I optimized three parameters: Josephson, charging, and inductive energy while keeping the external flux steady at 0.5. This test yielded a lower coherence time than "TEST F" but increased anharmonicity.

Figure 6.29 shows the wavefunction representation of these tested circuits. "TEST F" showed promising results regarding coherence time, though its experimental feasibility is in question due to the low anharmonicity, making it more harmonic. The optimal values for both tests, as shown in Figure 6.30, reveal very low values, which could pose issues when driving the frequency for the qubit. Despite this, the resulting optimized values produced a double-well potential and achieved an enormous coherence time of 2.75 milliseconds. Theoretically, this optimization found optimal values for higher coherence times than those discovered experimentally, which is 1.48 milliseconds [32]. However, challenges may arise in experimentation, particularly regarding the low anharmonicity, indicating convergence to the a harmonic oscillator shape of the double-well potentials.

In Figure 6.29, the second test, "TEST D," has a shorter coherence time but appears more stable and more anharmonic than "TEST F.

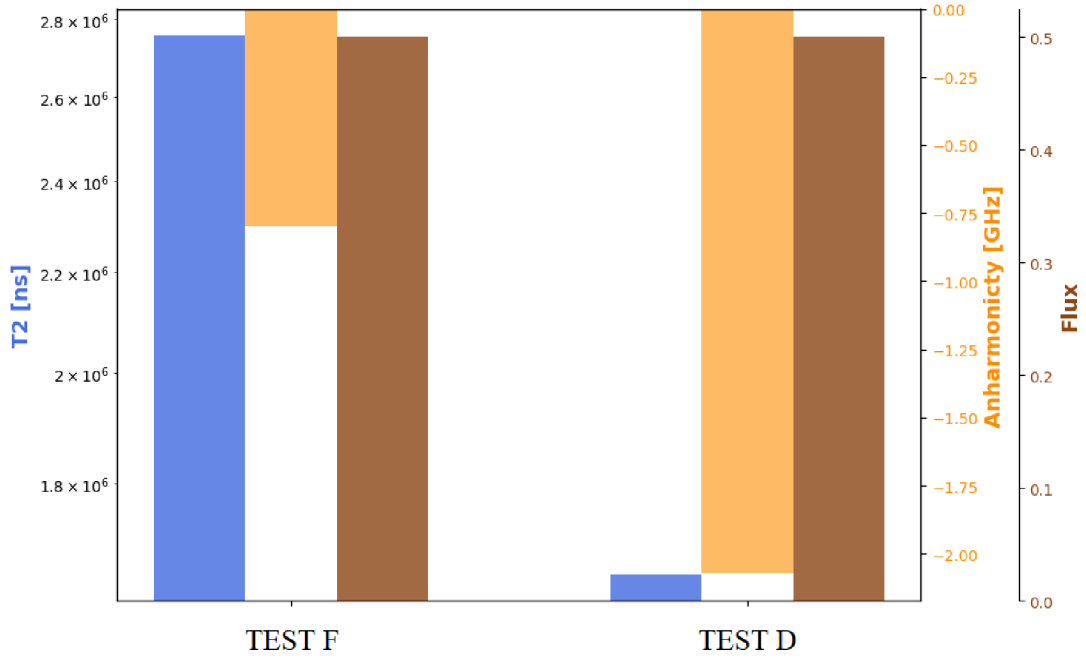

Figure 6.28: T4 circuit results - (coherence time (T_2), anharmonicity (α), and flux). The optimization for 'TEST F' yielded the longest coherence time. 'TEST D' demonstrates characteristics potentially suitable for this qubit. Numerical values are shown in Figure 6.26.

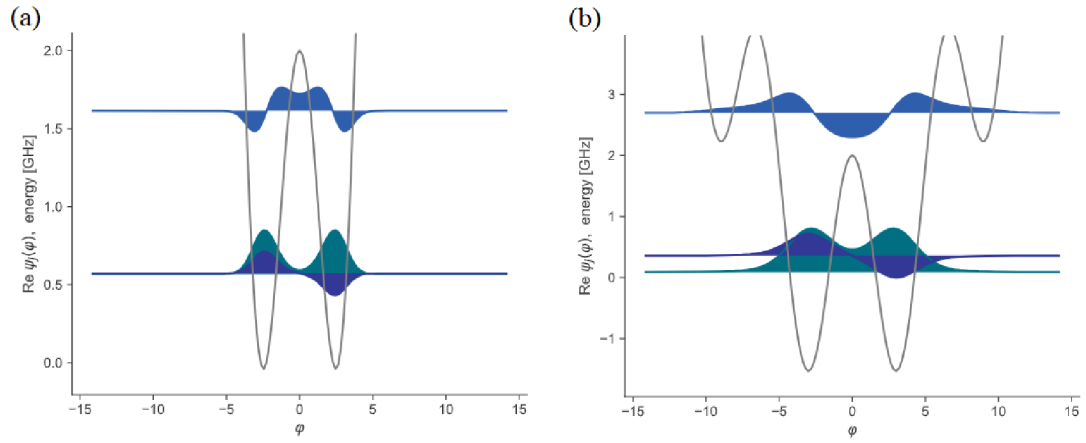

Figure 6.29: T4 circuit - wavefunction representation for (a) TEST F and (b) TEST D.

	EJ	EC	EL	φ	T2	α
TEST F	2.04234	0.10059	0.5	0.5	2756502	-0.7962
TEST D	2.00746	1.0028	0.10008	0.5	1651305	-2.0695

Figure 6.30: T4 circuit - numerical results to "TEST F" and "TEST D".

6.3.6 T5 circuit - results and discussion

The T5 circuit represents a well-known qubit known as Transmon, introduced in Section 4.2, with various optimizations discussed in Section 6.1. As depicted in Figure 6.31, the circuit consists of symbolized Josephson junctions, denoting the Transmon circuit design. The expected behavior of this qubit is to achieve a very high ratio $E_J/E_C >> 1$, placing it in the flux regime. I want to find optimal values that achieve a coherence time greater than 0.5 μm, as achieved for relaxation time T_1 in [33]. The results for the most promising testing are visually depicted in Figures 6.32 and 6.34, with their corresponding numerical representation provided in Figure 6.35.

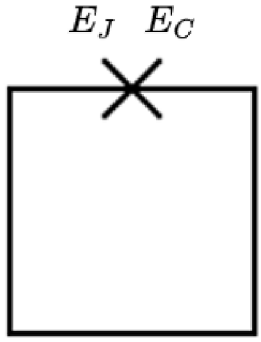

Figure 6.31: T5 circuit contains 2 parameters: E_J and E_C .

In "TEST F," a meticulous optimization strategy was employed, targeting Josephson and charging energies with 300 points and double optimization runs. This rigorous approach was complemented by expansive parameter bounds, allowing for a thorough exploration of the parameter space. As depicted in Figure 6.32, the outcome revealed a remarkable achievement: a substantial increase in coherence time.

Additionally, the analysis unveiled intriguing insights into the qubit's behavior. Despite the impressive coherence time, the observed anharmonicity trended towards the lower spectrum, suggesting a more harmonic oscillator-like behavior. This inference was substantiated by the cosine-like well structure displayed in Figure 6.33, underscoring the qubit's nuanced energy landscape.

Furthermore, an examination of the ratio values, as illustrated in Figure 6.34, revealed a convergence towards a specific range, consistent with previous Transmon optimization studies. Interestingly, a similar ratio pattern emerged in the secondary "test E," suggesting potential viability despite differences in coherence time outcomes. While "TEST F" displayed superior coherence time, "TEST E" exhibited comparable energy level structures, albeit with lower coherence time values, as indicated in Figure 6.32.

Figure 6.32 shows tests for the optimization runs of the T5 circuit. Ultimately, "Test F" emerged as the most promising iteration, boasting exceptional coherence time results. Despite the near-harmonic regime, the attained parameter values aligned closely with expected qubit characteristics.

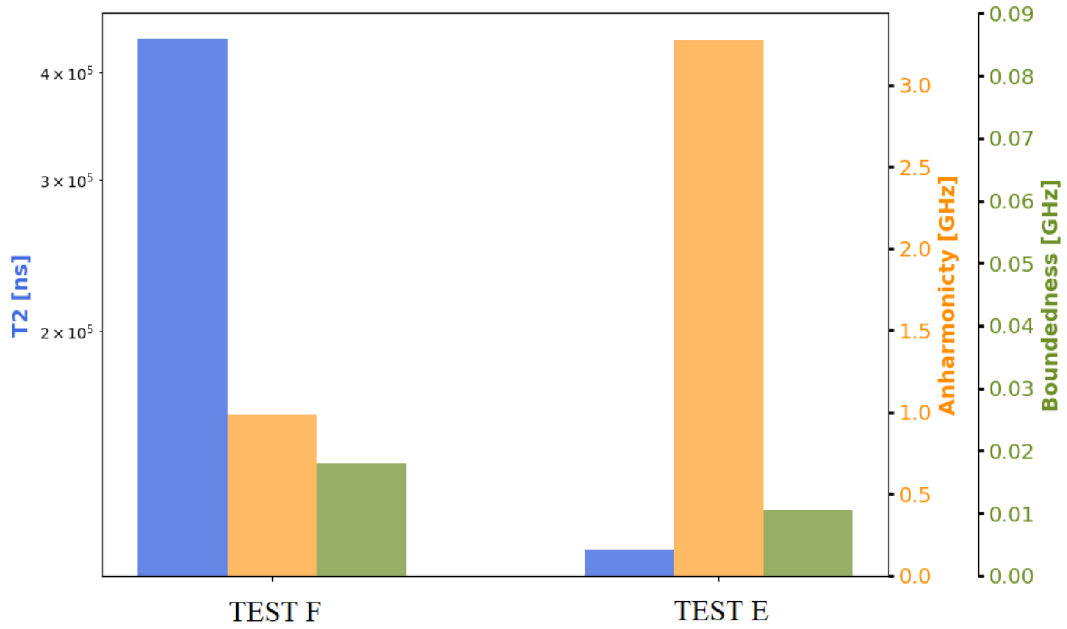

Figure 6.32: T5 circuit - results (coherence time (T_2), anharmonicity (α), and boundedness (B)). The optimization for "TEST F" yielded the longest coherence time. "TEST E" demonstrates characteristics potentially suitable for this qubit. Numerical values are shown in Figure 6.35.

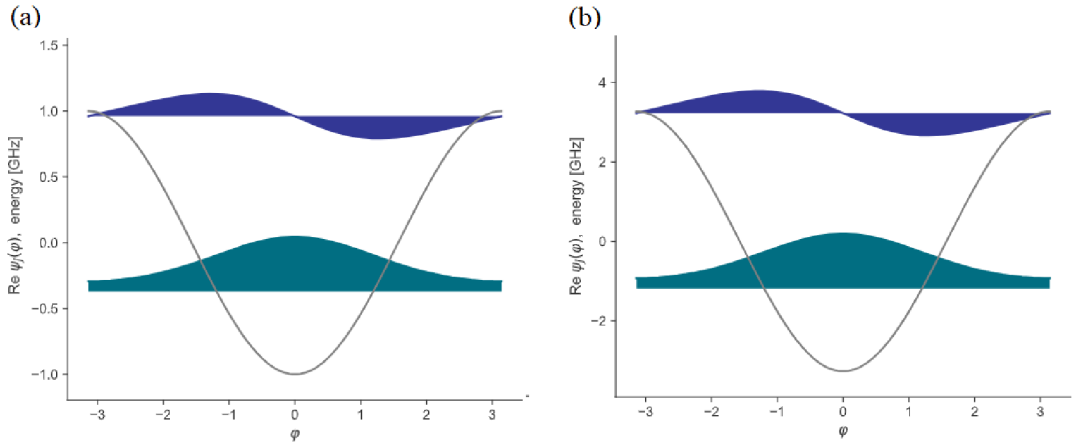

Figure 6.33: T5 circuit - wavefunction representation for (a) TEST F and (b) TEST E.

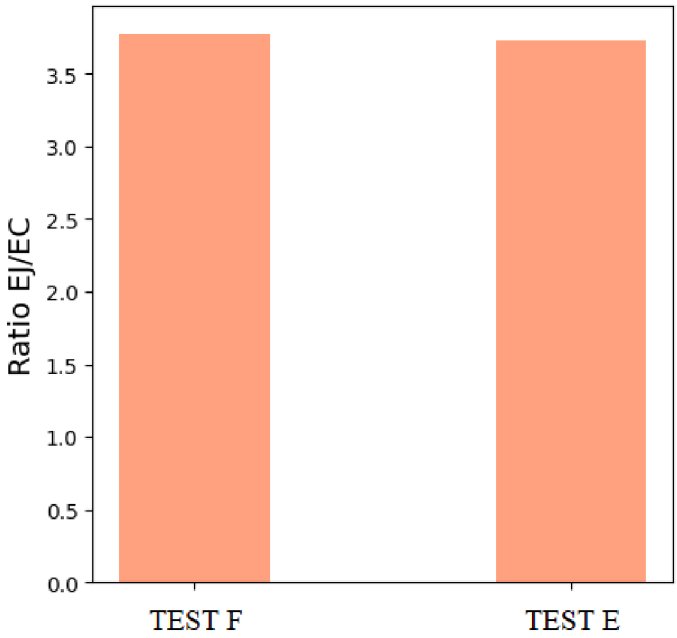

Figure 6.34: T5 circuit - the ratio of E_J/E_C results for two tests, "TEST F" and "TEST E". Numerical values are shown in Figure 6.35.

	EJ	EC	EJ/EC	T2	α	B
TEST F	1.00119	0.2652	3.77522	437462.7	0.98609	0.01796
TEST E	3.27608	0.87906	3.72682	111446.8	3.27456	0.01051

Figure 6.35: T5 circuit - numerical results for the optimizations of "TEST F" and "TEST E".

6.3.7 T6 circuit - results and discussion

The final test circuit, T5, integrates a Transmon circuit with an added capacitor and inductor, eliminating the need for external magnetic flux. In this configuration, the capacitor should not influence much since the Josephson junction symbolizes a Transmon circuit. Additionally, the inductor's role is crucial, as its low value ensures a shallow quadratic well potential, facilitating high anharmonicity and no deduction of boundedness for the circuit, which showed in the past couple of circuits to be an issue when deriving optimal values. Figure 6.36 visually depicts the T6 circuit. The outcomes of two tests, "TEST E" selected for its extended coherence time and "Test A" chosen for its viability, are illustrated in Figures 6.37 and 6.38. Their corresponding numerical data and optimal energy parameter values are also detailed in Figure 6.39.

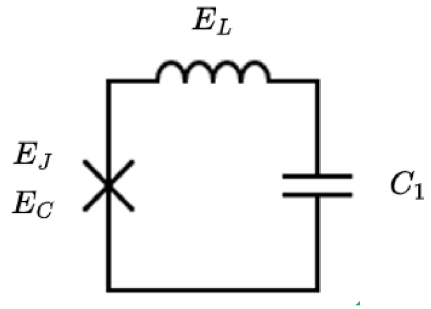

Figure 6.36: T6 circuit contains 4 parameters: E_J, E_C, E_L, and C_1.

In "TEST E," the optimization strategy focused on setting broad bounds for E_J and C_1 while maintaining constant values for the charging energy E_C of the Josephson junction and the inductive energy E_L. This approach yielded a remarkably extended coherence time, as depicted in Figure 6.37. However, despite the seemingly large anharmonicity observed, it is relatively low, indicating that the circuit behaves more like a harmonic oscillator. This inference is reinforced by the ratio in Figure 6.38, which suggests that the Josephson junction operates within the charging regime. Additionally, the numerical analysis of optimal values in Figure 6.39 reveals that E_J is significantly smaller than E_L, resulting in a predominantly quadratic well and hence a harmonic oscillator.

In contrast, "TEST A" resulted in more promising outcomes. Here, no fixed values were set, allowing all parameters to be optimized with relatively loose bounds for the Josephson junction and slightly tighter constraints for the capacitor, while the inductor had reasonable bounds. Despite achieving a notably lower coherence time and anharmonicity compared to the previous test, as illustrated in Figure 6.37, the derived parameter values for the inductive energy and capacitor, depicted in Figures 6.38 and 6.39, respectively, appear more sensible. Particularly noteworthy is the significantly higher ratio of the Josephson junction, indicating operation in the flux regime. This suggests that "TEST A" may offer a more viable qubit configuration than "TEST E." However, the low anharmonicity and non-groundbreaking coherence time of "TEST A" raise questions about its potential for further exploration.

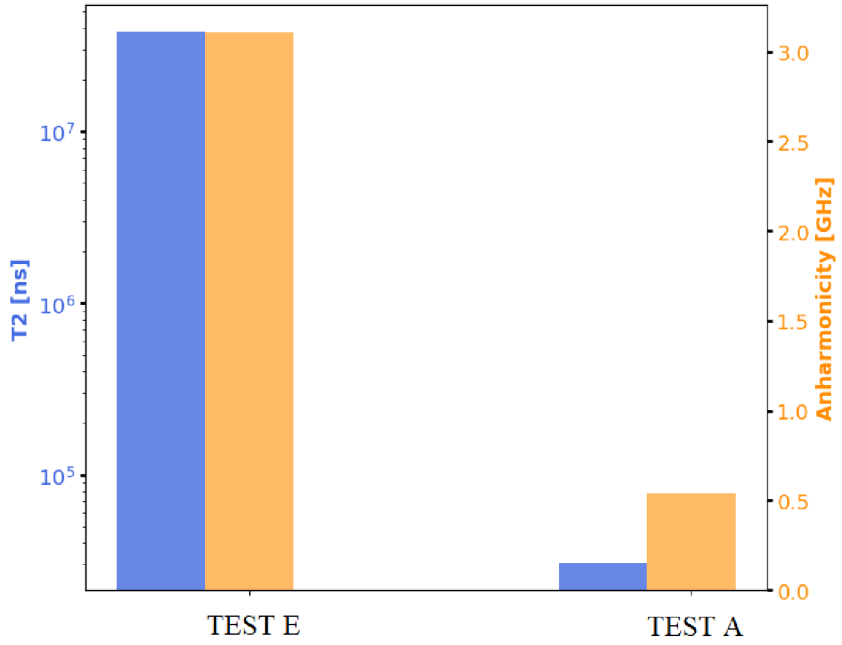

Figure 6.37: T6 circuit - results (coherence time (T_2), anharmonicity (α), and boundedness (B)). The optimization for 'TEST E' yielded the longest coherence time. 'TEST A' demonstrates characteristics potentially suitable for this qubit. Numerical values are shown in Figure 6.39.

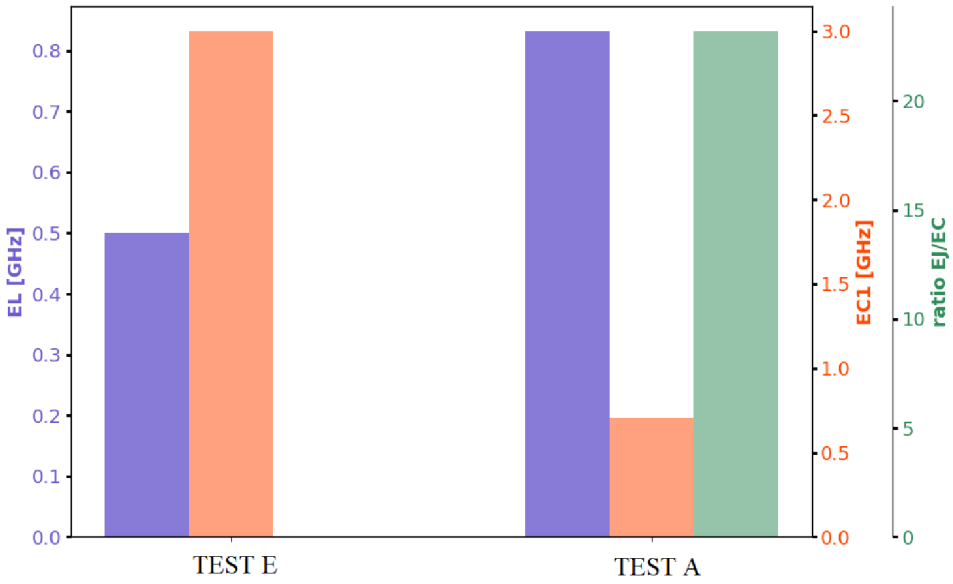

Figure 6.38: T6 circuit - the ratio of E_J/E_C results for two tests "TEST E" and "TEST A." Showcasing also values of inductor E_L and capacitor C_1 Numerical values are shown in Figure 6.35. Numerical values are shown in Figure 6.39.

	EJ	EC	EL	EC1	T2	α	EJ/EC
TEST E	0.02411	1	0.5	2.99814	38180277	3.10483	0.02411
TEST A	3.87407	0.16712	0.83162	0.70711	30431.91	0.53753	23.182

Figure 6.39: T6 circuit - numerical results for "TEST E" and "TEST A".

Conclusion

In this study, I demonstrated the successful optimization of various circuit layouts, resulting in enhanced coherence times and the identification of new optimal parameter values. The tests provided valuable insights into how specific bounds can guide the circuit's functioning as either a harmonic oscillator or a distinct qubit state. Furthermore, the analysis revealed that additional Josephson junctions necessitate reconsidering boundedness parameters in the absence of inductors. These findings contribute to the broader understanding of superconducting qubit design and optimization.

In optimizing circuit T0, I explored various bounds and cost function manipulations. The primary challenge was reducing boundedness to zero, which proved nearly impossible. When boundedness approached zero, it also caused the two Josephson junctions to converge to zero, resulting in a circuit that exhibited Transmon characteristics rather than the desired behavior.

Optimization of circuit T1 did not yield beneficial results either. While boundedness was not as problematic, the anharmonicity remained excessively high, consistently falling between 7-11 GHz, despite various interactions with energy parameters. The only instance of deriving acceptable values occurred with an optimization run using only two points, which is not valid.

In circuit T2, where an inductor was incorporated, the optimization struggled to achieve overall convergence. Free-bound conditions led the circuit to behave as a harmonic oscillator, characterized by high inductor values and low Josephson junction ratios, mainly when the external magnetic flux was set at the sweet spot 0.5.

Circuit T3 demonstrated significant potential for long coherence times due to its SQUID-like layout. When the charging energies for both junctions were fixed, the circuit delivered low ratios in the mid-flux and charging regimes and very high coherence times. When ratios were increased, increased boundedness and decreased coherence time were achieved. Even when the external magnetic flux was fixed at 0.5, the circuit failed to exhibit SQUID-like characteristics, suggesting issues with boundedness.

The Fluxonium circuit (T4) provided surprisingly positive results. It was possible to achieve coherence times longer than those experimentally observed, reaching 2.7 milliseconds compared to the known 1.48 milliseconds. The main question lies in the feasibility of engineering and fabrication. Theoretically, this qubit appears promising despite its borderline anharmonicity, occasionally leaning towards harmonic oscillator or Transmon behavior.

The well-known Transmon qubit (T5) had limited parameter modifications but yielded consistent results. High ratios reduced anharmonicity and increased coherence time, while lower ratios increased anharmonicity but resulted in shorter coherence times. The relationship between parameters consistently indicated Transmon characteristics.

Circuit T6 presented difficulties, often converging to undefined eigenstates. Limited testing revealed no consistency or potential for exceptionally high coherence times. The only long coherence times occurred when the circuit behaved as a harmonic oscillator influenced by the inductor. The inductor's tendency to promote harmonic behavior highlights the need for strict bounds to maintain anharmonicity.

After numerous optimization processes and variations for each circuit (T0-T6), I compared the longest coherence times in Figure 6.40. Although focused solely on coherence time rather than feasibility, circuit T3 was expected to achieve the longest coherence time, highlighted in Figure 6.40 with dark fuchsia color. These findings provide valuable insights into the optimization and potential of different qubit circuits, highlighting both theoretical possibilities and practical challenges.

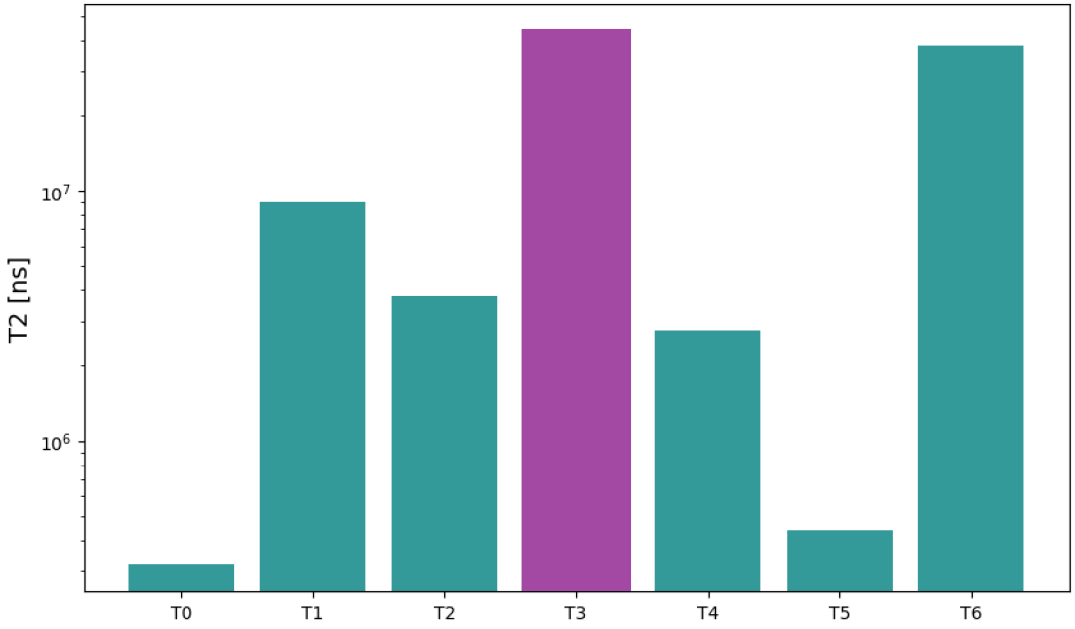

Figure 6.40: All circuits combined with their longest coherence times T_2. The winner (purler bar) for the longest coherence time T_2 is "TEST A" for circuit T3. Numerical results are shown in Figure 6.42.

On the other hand, Figure 6.41 shows all the previously discussed doable circuits. Some circuits may not be appropriately configured due to boundedness issues in the cost function, particularly those with more than one Josephson junction. These circuits resulted in significantly higher unboundedness and were pushed to regions with low coherence time to satisfy the boundedness condition. Despite this challenge, the circuit with the longest coherence time is assumed to be T4, Fluxonium. This circuit has one Josephson junction and an inductor element, so boundedness is not calculated.

Circuits T0, T1, and T3 have evident challenges and significant effects caused by boundedness. If boundedness were not an issue, it is likely that circuit T3, the SQUID-like shaped qubit, would converge to have the highest coherence time. Nevertheless, Fluxonium T4 exhibits the longest coherence time among the doable circuits, as shown in Figure 6.41. This finding encourages further experimentation and analysis for Fluxonium, as it has demonstrated new and longer coherence times than those previously tested experimentally, as illustrated in Figure 6.40. Corresponding numerical results for the coherence

times can be found in Figure 6.42.

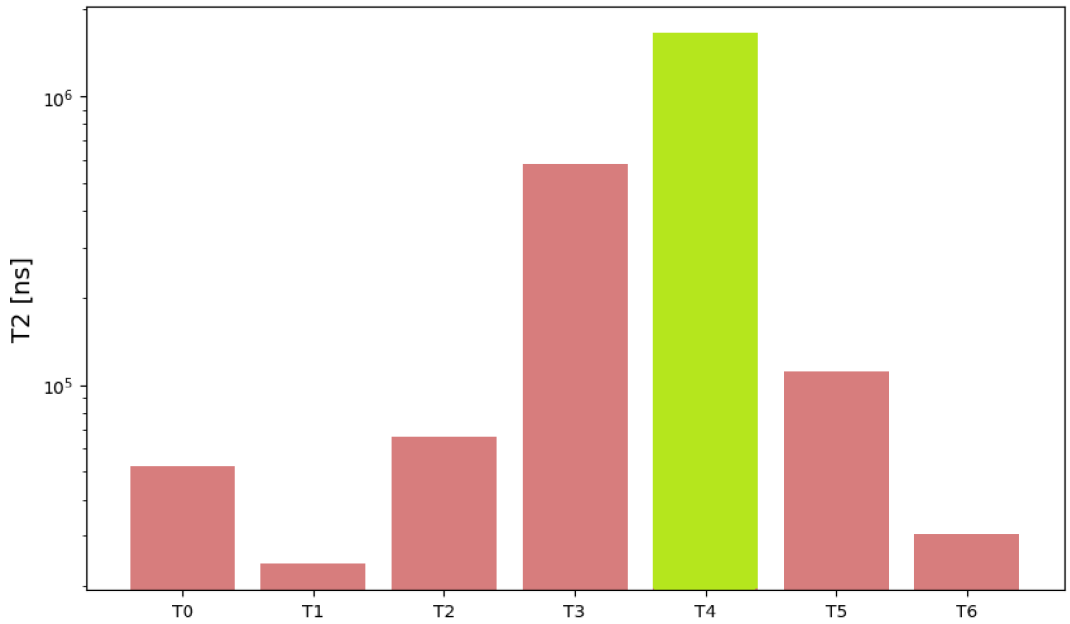

Figure 6.41: All circuits combined based on their potential feasibility T_2. The winner (green color) for coherence time T_2 is "TEST D" for circuit T4 with the longest coherence time. Numerical results are shown in Figure 6.42.

	(a) T2 [ns]	(b) T2 [ns]
T0	318792.514	52381.199
T1	8966032.87	23998.635
T2	3762673.77	66213.254
T3	43580435.8	582524.13
T4	2756502.3	1651304.5
T5	437462.695	111446.83
T6	38180276.6	30431.908

Figure 6.42: All circuits combined and their coherence times. (a) Circuit with their longest coherence times. (b) Circuit with their coherence times but based on potential feasibility.

Bibliography

[1] Martina Gschwendtner, Nicole Morgan, and Henning Soller. *Quantum technology use cases as fuel for value in finance*. 2023. URL: https://www.mckinsey.com/capabilities/mckinsey-digital/our-insights/tech-forward/quantum-technology-use-cases-as-fuel-for-value-in-finance.

[2] Dorothy E. Denning. "Is Quantum Computing a Cybersecurity Threat?" In: *American Scientist* 107.2 (2019). DOI: 10.1511/2019.107.2.83.

[3] Norbert M. Linke et al. "Experimental comparison of two quantum computing architectures". In: *Proceedings of the National Academy of Sciences* 114.13 (2017), pp. 3305–3310. DOI: 10.1073/pnas.1618020114. eprint: https://www.pnas.org/doi/pdf/10.1073/pnas.1618020114. URL: https://www.pnas.org/doi/abs/10.1073/pnas.1618020114.

[4] Zahid Hussain. "Strengths and Weaknesses of Quantum Computing." In: *International Journal of Scientific and Engineering Research* 7 (Sept. 2016). URL: https://www.researchgate.net/publication/308414229_Strengths_and_Weaknesses_of_Quantum_Computing.

[5] Tim Forcer et al. "Superposition, Entanglement and Quantum Computation". In: *Quantum Information Computation* 2 (Mar. 2002). DOI: 10.26421/QIC2.2-1.

[6] Wazir Khan et al. "Quantum Cryptography a Real Threat to Classical Blockchain: Requirements and Challenges". In: (Oct. 2022). DOI: 10.36227/techrxiv.21341817.v1.

[7] Alexandre Blais et al. "Circuit quantum electrodynamics". In: *Reviews of Modern Physics* 93.2 (May 2021). ISSN: 1539-0756. DOI: 10.1103/revmodphys.93.025005. URL: http://dx.doi.org/10.1103/RevModPhys.93.025005.

[8] P. Krantz et al. "A quantum engineer's guide to superconducting qubits". In: *Applied Physics Reviews* 6.2 (June 2019). ISSN: 1931-9401. DOI: 10.1063/1.5089550. URL: http://dx.doi.org/10.1063/1.5089550.

[9] Morten Kjaergaard et al. "Superconducting Qubits: Current State of Play". In: *Annual Review of Condensed Matter Physics* 11.1 (Mar. 2020), 369–395. ISSN: 1947-5462. DOI: 10.1146/annurev-conmatphys-031119-050605. URL: http://dx.doi.org/10.1146/annurev-conmatphys-031119-050605.

[10] S.E. Rasmussen et al. "Superconducting Circuit Companion—an Introduction with Worked Examples". In: *PRX Quantum* 2 (4 2021), p. 040204. DOI: 10.1103/PRXQuantum.2.040204. URL: https://link.aps.org/doi/10.1103/PRXQuantum.2.040204.

[11] *The Capacitor Handbook*. 2024. URL: http://archive.org/details/the-capacitor-handbook.

[12] K. Kawabe, H. Koyama, and K. Shirae. "Planar inductor". In: *IEEE Transactions on Magnetics* 20.5 (1984), pp. 1804–1806. DOI: 10.1109/TMAG.1984.1063271.

[13] John M. Martinis and Kevin Osborne. *Superconducting Qubits and the Physics of Josephson Junctions*. 2004. arXiv: cond-mat/0402415 [cond-mat.supr-con].

[14] Michael Tinkham. *Introduction to superconductivity*. Courier Corporation, 2004.

[15] Antonio Vettoliere, Paolo Silvestrini, and Carmine Granata. "3 - Superconducting quantum magnetic sensing". In: *Quantum Materials, Devices, and Applications*. Ed. by Mohamed Henini and Marcelo Oliveira Rodrigues. Elsevier, 2023, pp. 43–85. ISBN: 978-0-12-820566-2. DOI: https://doi.org/10.1016/B978-0-12-820566-2.00001-6. URL: https://www.sciencedirect.com/science/article/pii/B9780128205662000016.

[16] Nathan K. Langford. *Circuit QED - Lecture Notes*. 2013. arXiv: 1310.1897 [quant-ph].

[17] S. M. Girvin. "113Circuit QED: superconducting qubits coupled to microwave photons". In: *Quantum Machines: Measurement and Control of Engineered Quantum Systems: Lecture Notes of the Les Houches Summer School: Volume 96, July 2011*. Oxford University Press, June 2014. ISBN: 9780199681181. DOI: 10.1093/acprof:oso/9780199681181.003.0003. eprint: https://academic.oup.com/book/0/chapter/367194888/chapter-pdf/45138561/acprof-9780199681181-chapter-3.pdf. URL: https://doi.org/10.1093/acprof:oso/9780199681181.003.0003.

[18] Alessandro Ciani, David P. Divincenzo, and Barbara M. Terhal. 2024. URL: https://textbooks.open.tudelft.nl/textbooks/catalog/book/85.

[19] Samuel J. Ling, Jeff Sanny, and William Moebs. *The Quantum Harmonic Oscillator*. URL: https://pressbooks.online.ucf.edu/osuniversityphysics3/chapter/the-quantum-harmonic-oscillator/.

[20] David J. Griffiths and Darrell F. Schroeter. *Introduction to quantum mechanics*. Third edition. Cambridge ; New York, NY: Cambridge University Press, 2018. ISBN: 978-1-107-18963-8.

[21] R. M. Lutchyn, L. I. Glazman, and A. I. Larkin. "Kinetics of the superconducting charge qubit in the presence of a quasiparticle". In: *Phys. Rev. B* 74 (6 2006), p. 064515. DOI: 10.1103/PhysRevB.74.064515. URL: https://link.aps.org/doi/10.1103/PhysRevB.74.064515.

[22] Uri Vool and Michel Devoret. "Introduction to quantum electromagnetic circuits". In: *International Journal of Circuit Theory and Applications* 45.7 (June 2017), 897–934. ISSN: 1097-007X. DOI: 10.1002/cta.2359. URL: http://dx.doi.org/10.1002/cta.2359.

[23] Jens Koch et al. "Charge-insensitive qubit design derived from the Cooper pair box". In: *Phys. Rev. A* 76 (4 2007), p. 042319. DOI: 10.1103/PhysRevA.76.042319. URL: https://link.aps.org/doi/10.1103/PhysRevA.76.042319.

[24] Thomas E. Roth, Ruichao Ma, and Weng C. Chew. "The Transmon Qubit for Electromagnetics Engineers: An introduction". In: *IEEE Antennas and Propagation Magazine* 65.2 (Apr. 2023), 8–20. ISSN: 1558-4143. DOI: 10.1109/map.2022.3176593. URL: http://dx.doi.org/10.1109/MAP.2022.3176593.

[25] Vladimir E Manucharyan et al. "Fluxonium: Single cooper-pair circuit free of charge offsets". In: *Science* 326.5949 (2009), pp. 113–116.

[26] Nicholas A. Masluk et al. "Microwave Characterization of Josephson Junction Arrays: Implementing a Low Loss Superinductance". In: *Phys. Rev. Lett.* 109 (13 2012), p. 137002. DOI: 10.1103/PhysRevLett.109.137002. URL: https://link.aps.org/doi/10.1103/PhysRevLett.109.137002.

[27] Farida Setiawan et al. "Analytic Design of Accelerated Adiabatic Gates in Realistic Qubits: General Theory and Applications to Superconducting Circuits". In: *PRX Quantum* 2 (July 2021). DOI: 10.1103/PRXQuantum.2.030306.

[28] Long B. Nguyen et al. "High-Coherence Fluxonium Qubit". In: *Phys. Rev. X* 9 (4 2019), p. 041041. DOI: 10.1103/PhysRevX.9.041041. URL: https://link.aps.org/doi/10.1103/PhysRevX.9.041041.

[29] Jens Koch et al. "Charging Effects in the Inductively Shunted Josephson Junction". In: *Physical Review Letters* 103.21 (Nov. 2009). ISSN: 1079-7114. DOI: 10.1103/physrevlett.103.217004. URL: http://dx.doi.org/10.1103/PhysRevLett.103.217004.

[30] Peter Groszkowski and Jens Koch. "Scqubits: a Python package for superconducting qubits". In: *Quantum* 5 (Nov. 2021), p. 583. ISSN: 2521-327X. DOI: 10.22331/q-2021-11-17-583. URL: http://dx.doi.org/10.22331/q-2021-11-17-583.

[31] F. Wilhelm and Koichi Semba. "Superconducting Quantum Computing: Status and Prospects". In: *World Scientific, 2006* 14 (Mar. 2006). DOI: 10.1142/9789812774705_0003.

[32] Aaron Somoroff et al. "Millisecond Coherence in a Superconducting Qubit". In: *Phys. Rev. Lett.* 130 (26 2023), p. 267001. DOI: 10.1103/PhysRevLett.130.267001. URL: https://link.aps.org/doi/10.1103/PhysRevLett.130.267001.

[33] Chenlu Wang et al. "Towards practical quantum computers: Transmon qubit with a lifetime approaching 0.5 milliseconds". In: *npj Quantum Information* 8.1 (2022), p. 3.